

Pitch-axis supermanoeuvrability in a biomimetic morphing-wing UAV

Arion Pons^{1,2,*} and Fehmi Cirak²

¹ Division of Fluid Dynamics, Department of Mechanics and Maritime Sciences, Chalmers University of Technology, Gothenburg 412 96, Sweden

² Department of Engineering, University of Cambridge, Cambridge CB2 1PZ, UK

Abstract

Birds and bats are extraordinarily adept flyers: whether in hunting prey, or evading predators, agility and manoeuvrability in flight are vital. In conventional high-performance aircraft, approaches to extreme manoeuvrability, such as post-stall manoeuvring, have often focused on thrust-vectoring technology – the domain of classical supermanoeuvrability – rather than biomimicry. In this work, however, we show that these approaches are not incompatible: biomimetic wing morphing is an avenue both to classical supermanoeuvrability, and to new forms of biologically-inspired supermanoeuvrability. Using a flight simulator equipped with a multibody model of lifting surface motion and a Goman-Khrabrov dynamic stall model for all lifting surfaces, we demonstrate the capability of a biomimetic morphing-wing unmanned aerial vehicles (UAV) for two key forms of supermanoeuvrability: the Pugachev cobra, and ballistic transition. Conclusions are drawn as to the mechanism by which these manoeuvres can be performed, and their feasibility in practical biomimetic unmanned aerial vehicle (UAV). These conclusions have wide relevance to both the design of supermanoeuvrable UAVs, and the study of biological flight dynamics across species.

Keywords: biomimetic aircraft, morphing wing, UAV, manoeuvrability, dynamic stall

1. Introduction

Birds, bats and other flying creatures show manoeuvrability beyond the performance of conventional fixed-wing uncrewed aerial vehicles (UAVs) of comparable scale. Manoeuvres such as perching [1–5], stall turns [6–8], whiffling [9], zero-air-speed rolling [10] and ballistic braking [11–13] all challenge the performance limits of conventional aircraft. Many natural flying creatures could indeed be characterized as *supermanoeuvrable*, defined in the classical sense by Herbst [14] and Gal-Or [15]: showing high angle-of-attack manoeuvrability and/or orientation control independent of flight path. The capabilities of modern supermanoeuvrable

* *E-mail:* arion@chalmers.se

jet aircraft, however, derive not from biomimicry but instead from the development of vectored propulsion, and advances in the study of unstable airframes [16]. In the late 1970s the Sukhoi Su-27 carried out the *Pugachev Cobra*, consisting of rapid pitch-up motion to beyond stall and then back again: an ability achieved simply by structural and aerodynamic design, including large wing strake, nose chines, and an unstable airframe [17,18]. With the addition of vectored propulsion systems, a wide range of further forms of supermanoeuvrability were enabled [14,15], and such systems are now a standard feature of high-performance jet aircraft [17].

Yet the problem and potential of biomimetic supermanoeuvrability remains. Several avenues of biomimetic research offer the potential for significant enhancements in the manoeuvrability of smaller-scale UAVs. In flapping-wing UAVs, it is possible to conceive of a biological mechanism of supermanoeuvrability that is analogous to conventional thrust vectoring: the vectoring of flapping-wing thrust via the alteration of wingbeat kinematics [19,20]. The scope for biomimicry in propulsive flapping is vast: among the vertebrate-inspired craft alone there are mimetic hummingbirds [21,22], seagulls [23,24], bats [25,26], pterosaurs [27], and more [28]. However, evidence from both extant and extinct species also suggests that the mechanisms of flapping-wing propulsion and supermanoeuvrability are not necessarily identical. Gliding mammals, which are without any form of aerial propulsion, show capability for manoeuvres – ostensibly supermanoeuvres – such as stall turning and ballistic braking [11–13,29–31]. Several species of birds can carry out zero-air-speed rolling and perching manoeuvres without flapping motion [5,10], and evolutionary studies indicate that in the lineage of birds, flight manoeuvrability evolved before a strong power stroke [32].

A pertinent question is thus whether biological and/or conventional forms of supermanoeuvrability could be achieved in a UAV with only non-propulsive biomimetic wing morphing. Through a simulation-based case study of such a UAV, we answer this question in the affirmative: several forms of pitch-axis supermanoeuvrability, including both the classical Pugachev Cobra and bio-inspired ballistic transition manoeuvres, are enabled by wing morphing. Moreover, this supermanoeuvrability is enabled in UAV which is flight dynamically stable during level flight, and which is equipped with only a modest propulsion system (thrust-to-weight ratio $T/W = 0.5$). These results demonstrate that biomimetic wing morphing is an avenue to both biomimetic *and* classical supermanoeuvrability. In doing so, they both elucidate the mechanisms of animal post-stall flight manoeuvrability; and offer pathways for the enhancement of artificially-intelligent UAVs for dogfighting [33].

2. Flight simulation framework

2.1. Biomimetic UAV specification

As a case study, we use the biomimetic morphing-wing UAV studied in simulation by Pons and Cirak [34,35], and illustrated in Fig. 1A. This UAV is of scale $c. 1\text{ m}$ – approximately equivalent to a range of biological flying creatures, and existing morphing-wing UAVs – and it utilises the aerofoils of the similarly-scaled ShowTime 50 (ST50) remote-control aircraft. Table 1 presents a detailed specification, and comparison, of the UAV’s airframe parameters. The UAV operates at a nominal chordwise Reynolds number of $\approx 300,000$, for flight at 30 m/s , that is, twice the stall speed of the unmorphed UAV [36]. The UAV is equipped with a conventional axial propulsion system (propellor, jet, *etc.* – we are agnostic as to its exact nature); as well as six-degree-of-freedom (6-DOF) wing morphing: asymmetric sweep, maximally-actuated configuration for scoping purposes – in the course of the analysis, we will identify which of these degrees of freedom are relevant to the pitch-axis supermanoeuvrability. Flight simulation routines for this UAV, based on a mesh of aerodynamic section models (Fig. 1C) interfaced with a multibody dynamic morphing model, have previously been developed

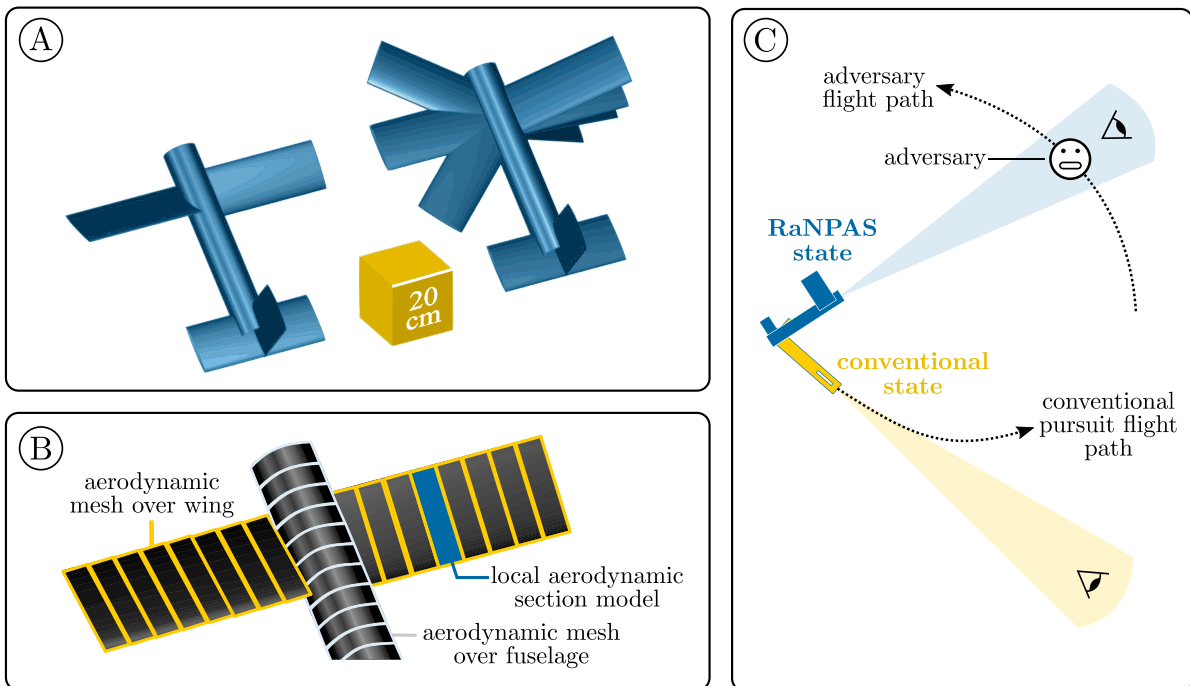


Figure 1: Illustration of the case study biomimetic morphing-wing UAV. (A) Morphing degrees of freedom of the case study UAV: wing incidence, sweep, and dihedral, all independently controllable on both wings. (C) Example mesh of aerodynamic models for the UAV. (B) Dogfighting context of a RaNPAS manoeuvre: the ability to significantly alter the UAV field of view, independent of the flight path.

and validated [34,35]. These simulation routines are valid for the UAV's angle-of-attack full-envelope, but only for quasisteady flight conditions: to extend flight simulation capability to the highly transient conditions of supermanoeuvres, such as the hypothetical pitch-axis RaNPAS manoeuvre illustrated in Fig. 1B, we will need to extend these routines.

2.2. Flight simulation framework

We begin with the flight simulation model framework developed in Pons and Cirak [34], which expresses this UAV's flight dynamics in a 12-DOF nonlinear state-space relation:

$$\mathbf{B}_1(\mathbf{z}, \mathbf{v})\dot{\mathbf{z}} = \mathbf{f}(\mathbf{z}, \mathbf{v}) - \mathbf{B}_0(\mathbf{z}, \mathbf{v})\mathbf{z}, \quad (1)$$

with state variable $\mathbf{z} \in \mathbb{R}^{12}$ encoding position and orientation values and rates; a set of N configuration and control parameters $\mathbf{v} \in \mathbb{R}^N$, accounting for morphing, propulsion, and other control surface (elevator/rudder) inputs; and matrix/vector functions $\mathbf{B}_1(\cdot)$, $\mathbf{B}_0(\cdot)$ and $\mathbf{f}(\cdot)$ describing the UAV multibody dynamics, aerodynamics, propulsion, and gravitational effects. Detailed definitions of $\mathbf{B}_1(\cdot)$, $\mathbf{B}_0(\cdot)$ and $\mathbf{f}(\cdot)$ are given in the Supplementary Material. Orientations are encoded in Euler angles: gimbal lock is bypassed through a pole-switching routine, in which two Euler angle parameterizations are used to maintain non-singularity over the complete orientation space. Within the model, a multibody dynamics submodel accounts for the complete inertial effects of morphing; and a mesh of aerodynamic section models (Fig. 1B) computes aerodynamic forces. This mesh of aerodynamic models contributes to the forces $\mathbf{f}(\cdot)$ within Eq. 1. Previous work [34,35] utilised nonlinear but quasisteady section models, but modelling highly-transient RaNPAS behaviour adequately requires higher-fidelity aerodynamic models. Several such models have been demonstrated in the literature for morphing-wing UAVs, among them: (i) computational fluid dynamics (CFD) simulations [9,37]; (ii) phenomenological dynamic stall and lift hysteresis models, such as the Goman-Khrabrov (GK) model [38–40]; and (iii) machine-learning models derived from CFD data [41,42]. To enable efficient exploration of a manoeuvre space, in the absence of existing high-fidelity data, we utilize a GK dynamic stall model for this UAV, accounting for strongly transient effects arising from aerofoil pitching motion. In the context of the pitch-axis supermanoeuvrability, this is anticipated to be the primary mode of aerofoil transience – and, as such, GK models have been previously utilized in the study of pitch-axis manoeuvrability in other morphing-wing UAVs [38,39].

Table 1: Case study UAV airframe parameters, with reference to existing UAVs and a species of bird, *cf.* [34]. “/” denotes unavailable data.

	This study	NextGen MFX-1	ShowTime 50	Greylag Goose (<i>A. Anser</i>)
Properties:	Values:			
Length – fuselage	1.20 m	2.1 m	1.51 m	<i>c.</i> 0.82 m
Length – wing to tail	0.80 m	<i>c.</i> 1.17 m	<i>c.</i> 0.94 m	/
Length – body radius	0.10 m	<i>c.</i> 0.15 m	<i>c.</i> 0.088 m	/
Span – wing	1.60 m	2.8 m	1.46 m	<i>c.</i> 1.62 m
Span – horz. stabilizer	0.80 m	/	<i>c.</i> 0.62 m	/
Span – vert. stabilizer	0.40 m	/	<i>c.</i> 0.17 m	/
Chord – wing	0.15 m	<i>c.</i> 0.23	0.32 m	<i>c.</i> 0.26 m
Chord – horz. stabilizer	0.15 m	/	<i>c.</i> 0.22 m	/
Chord – vert. stabilizer	0.15 m	/	<i>c.</i> 0.09 m	/
Mass – total	8 kg	45 kg	2.9 kg	<i>c.</i> 3.3 kg

3. Aerodynamic modelling of dynamic stall

3.1. Formulation

To account for the effects of dynamic stall, a modified Goman-Khrabrov (GK) model is implemented in the UAV’s mesh of section models, expanding on the work of Reich [38] and Pons and Cirak [43]. For each section model i across the UAV, the aerodynamic coefficients for force F (\in {lift, drag, pitching moment}) as a function of local angle-of-attack α , $C_{i,F}(\alpha_i)$, are given by:

$$C_{i,F}(\alpha_i) = p_i C_{i,F,\text{att}}(\alpha_i) + (1 - p_i) C_{i,F,\text{sep}}(\alpha_i), \quad (3)$$

where $C_{i,F,\text{att}}(\alpha_i)$ and $C_{i,F,\text{sep}}(\alpha_i)$ are the aerodynamic coefficient functions for the hypothetical cases of local attached and separated flow respectively. p_i are local dynamic mixing parameters, loosely connected to the location of the separation point along the aerofoil chord [44], and governed by the first-order differential equation:

$$\tau_{1,i} \dot{p}_i(\alpha_i) = p_{0,i}(\alpha_i - \tau_{2,i} \dot{\alpha}_i) - p_i(\alpha_i), \quad (4)$$

where α_i and $\dot{\alpha}_i$ are the local angle of attack and corresponding rate, $\tau_{1,i}$ and $\tau_{2,i}$ are delay parameters, and $p_{0,i}(\alpha)$ is a mixing function representing the transition between attached and separated flow. Accurate identification of the functions $C_{i,F,\text{att}}(\alpha_i)$, $C_{i,F,\text{sep}}(\alpha_i)$ and $p_{0,i}(\alpha_i)$, and the delays $\tau_{1,i}$ and $\tau_{2,i}$, are crucial to accurate dynamic stall modelling. Notably, the former three functions are identifiable based only on quasistatic aerodynamic data, for which $p_i = p_{0,i}$.

3.2. Wing quasisteady parameter identification

Quasistatic aerodynamic data for the UAV's aerofoils is given by Selig [45]: this includes the wing (ST50W) and stabiliser (ST50H) aerofoils, the latter additionally accounting for elevator and rudder deflections. Following Pons and Cirak [43], we begin with the simpler lifting surface: the wing. Curve fitting (Fig. 2) indicates that it is not well-approximated by flat-plate attached- and separated-flow models, *cf.* [38], but instead, is well-approximated by an alternative pair of models: **(i)** the separated flow model:

$$\begin{aligned} C_{i,L, \text{sep}}(\alpha_i) &= a_{i,L} \operatorname{sgn} \alpha_i \sin(b_{i,L} |\alpha_i + c_{i,L}| + d_{i,L}) + e_{i,L}, \\ C_{i,D, \text{sep}}(\alpha_i) &= a_{i,D} \sin(b_{i,D} |\alpha_i| + c_{i,D}) + d_{i,D}, \\ C_{i,M, \text{sep}}(\alpha_i) &= a_{i,M} \operatorname{sgn} \alpha_i \sin(b_{i,M} |\alpha_i + c_{i,M}| + d_{i,M}) + e_{i,M}, \end{aligned} \quad (5)$$

with angle-of-attack α_i , signum function $\operatorname{sgn}(\cdot)$, and model parameters $a_{i,j}$, $b_{i,j}$, $c_{i,j}$, $d_{i,j}$ and $e_{i,j}$; and **(ii)** the attached flow model:

$$\begin{aligned} C_{i,L, \text{att}}(\alpha_{l,i}) &= C_{i,L\alpha,l} \alpha_{l,i}, & C_{i,L, \text{att}}(\alpha_{t,i}) &= C_{i,L\alpha,t} \alpha_{t,i}, \\ C_{i,M, \text{att}}(\alpha_{l,i}) &= 0, & C_{i,M, \text{att}}(\alpha_{t,i}) &= C_{i,M\alpha,t} \alpha_{t,i}, \\ C_{i,D, \text{att}}(\alpha_{l,i}) &= 0, & C_{i,D, \text{att}}(\alpha_{t,i}) &= 0, \end{aligned} \quad (6)$$

with model parameters $C_{i,L\alpha,l}$, $C_{i,L\alpha,t}$ and $C_{i,M\alpha,t}$, and where $\alpha_{l,i}$ and $\alpha_{t,i}$ are the leading and trailing edge angles of attack – representing a partition of the full domain, $|\alpha_i| < 180^\circ$, into $|\alpha_i| \leq 90^\circ$ and $||\alpha_i| - 180^\circ| \leq 90^\circ$, the latter of which is mapped back to $|\alpha_i| \leq 90^\circ$ again. The separation of attached flow models into leading- and trailing-edge submodels accounts for the quantitative differences between forward and reverse flow over the aerofoil, and is a modification to existing GK-based flight simulation frameworks [38,39] to encompass a full flight envelope. Note, however, that we do not consider quasistatic hysteresis, because the aerofoil is thin [44]. As per Fig. 2, three of the attached flow models are observably near-zero; and values for other model parameters are identified via nonlinear least-squares regression applied to selections of manually-identified attached and separated flow.

Using these separated and attached flow models, it is then also possible to estimate a wing aerofoil mixing function $p_{0,i}(\alpha)$, by solving $p_i = p_{0,i}$ in Eq. 3. Figure 3 shows the results of this process, fitted to an arctangent expression for $p_{0,i}(\alpha_i)$ [38,40]:

$$p_{0,i}(\alpha_i) = \begin{cases} 1 & |\alpha_i| < 4^\circ \\ -0.0058 \tan^{-1}(|\alpha_i| + 16) & 4^\circ \leq |\alpha_i| \leq 32^\circ \\ 0 & |\alpha_i| > 32^\circ. \end{cases} \quad (7)$$

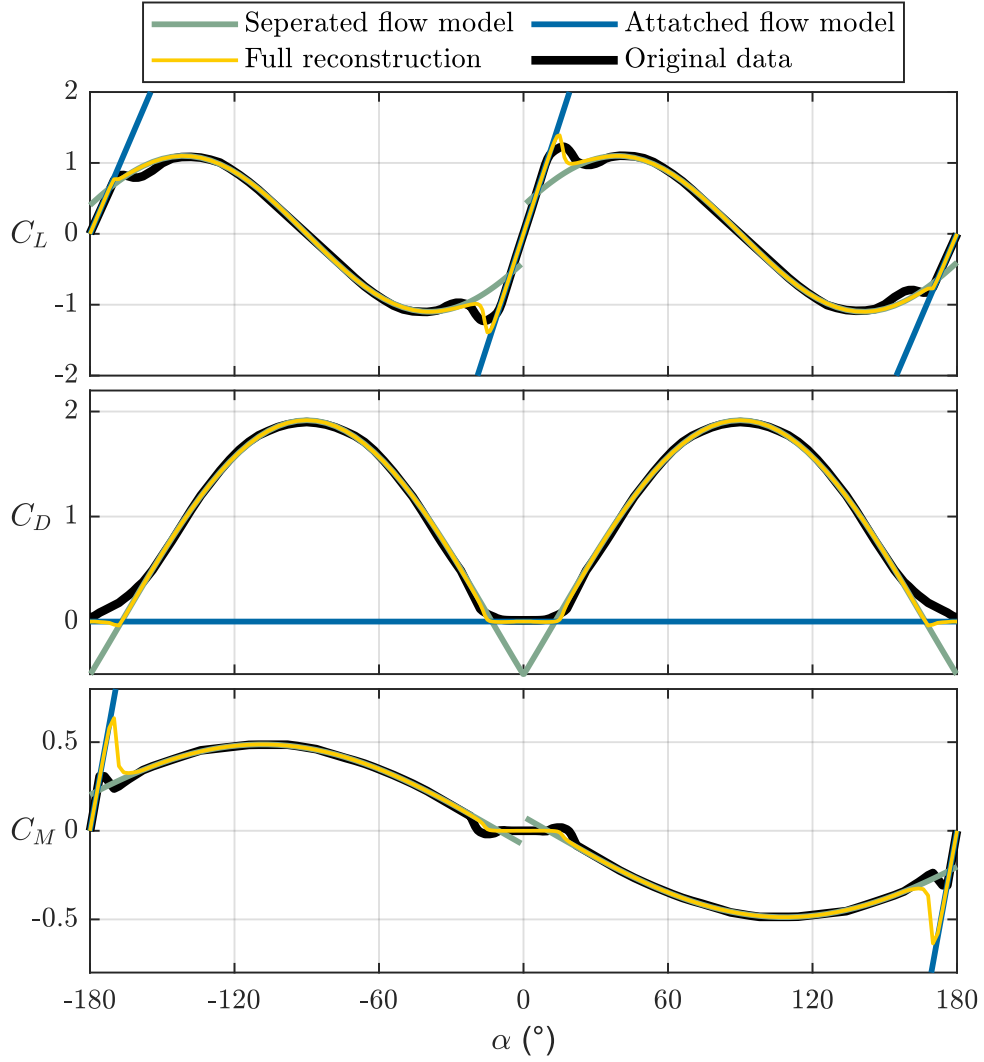


Figure 2: Quasisteady aerodynamic coefficient data for the wing aerofoil (ST50W), as a function of angle-of-attack (α), reconstructed from the GK attached and separated flow models, compared to the original data

which is reasonably accurate, particularly for drag and moment data. To accurately modify the trailing edge (Fig. 3), this expression is modified to account for earlier and faster separation:

$$p_{0,i}(\alpha_{t,i}) = \begin{cases} 1 & |\alpha_{t,i}| < 4^\circ \\ -0.0058 \tan^{-1}(1.6|\alpha_{t,i}| + 16) & 4^\circ \leq |\alpha_{t,i}| \leq 21^\circ \\ 0 & |\alpha_{t,i}| > 21^\circ. \end{cases} \quad (8)$$

Using the quasisteady coefficient models (Eq. 5-6) and mixing functions (Eq. 7-8), we may then reconstruct complete quasisteady coefficient data and validate it against the original data (Fig. 2). As per Pons and Cirak [43], the result is overall very good: the separated and attached flow regimes are modelled well. The most notable discrepancies are around the trailing edge transition in the drag and moment coefficients – as can be seen also in Fig. 3.

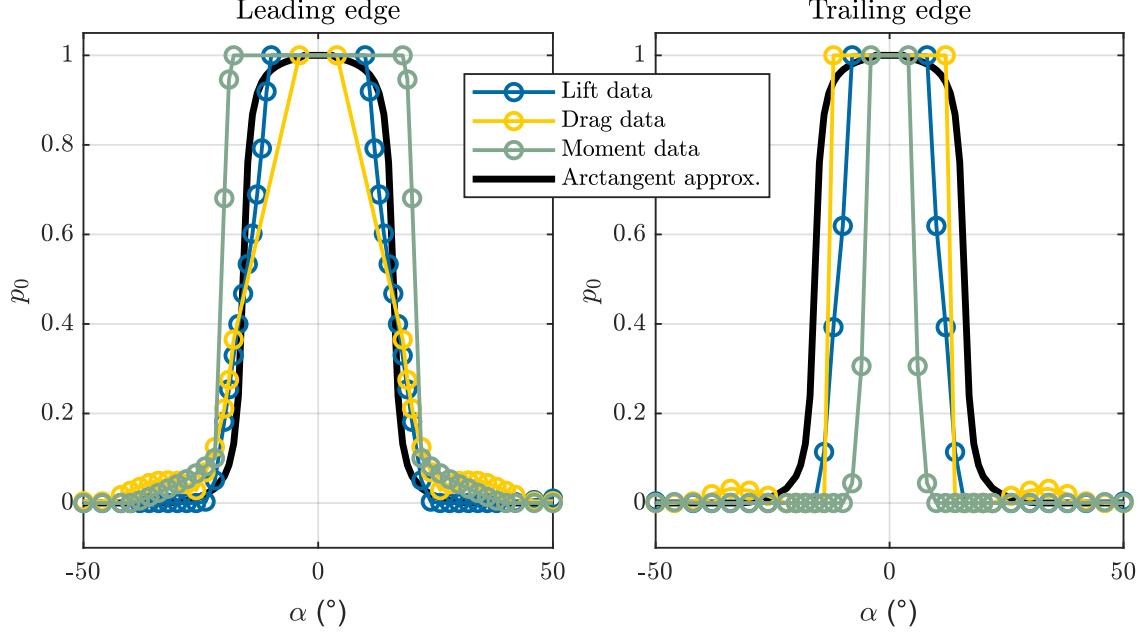


Figure 3: Filtered approximations to $p_{0,i}$ derived from wing aerofoil (ST50W) leading and trailing edge aerodynamic data, compared to the arctangent approximations.

3.3. Stabiliser dynamic parameter identification

Identifying GK quasistatic data for the stabilizer aerofoil (ST50H) is more difficult: this data presents the additional challenge of a dependence on the stabiliser control surface deflection. To begin, we assume quasistatic behaviour for the control surface motion – *i.e.*, that control surface motion itself induces no flow. Although the source dataset [45] contains aerodynamic coefficient data at seven different elevator deflections (-50° , -30° , -15° , 0° , 15° , 30° , 50°); only four of these are unique (*e.g.*, $\beta_e \in [-50, 0]^\circ$ or $\beta_e \in [0, 50]^\circ$). This is due to the symmetric aerofoil profile: downwards aerofoil motion at downwards control surface deflection is equivalent to upwards motion at upwards deflection. Selecting the unique set $\beta_e \in [-50, 0]^\circ$; for each control surface deflection data entry the attached and separated flow relations are identified according the separated-flow model:

$$\begin{aligned}
 C_{i,L,sep}(\alpha_i) &= a_{i,L} \operatorname{sgn}(\alpha_i + c_{i,L}) \sin(b_{i,L}|\alpha_i + c_{i,L}| + d_{i,L}) + e_{i,L}, \\
 C_{i,D,sep}(\alpha_i) &= \begin{cases} a_{i,D} \cos(b_{i,D}|\alpha_i + c_{i,D}| + d_{i,D}) + e_{i,D}, & \beta_e = 0 \\ a_{i,D} \sin(b_{i,D}\alpha_i + c_{i,D}) + d_{i,D} & \text{o.w.,} \end{cases} \quad (9) \\
 C_{i,M,sep}(\alpha_i) &= a_{i,M} \operatorname{sgn}(\alpha_i + c_{i,M}) \sin(b_{i,M}|\alpha_i + c_{i,M}| + d_{i,M}) + e_{i,M}.
 \end{aligned}$$

and the attached-flow model of Eq. 6. In Eq. 9, the sinusoid drag model at nonzero β_e makes the identification more robust: the complexity of the coefficient data does not permit an easy identification of more complex models. Model parameters are identified via nonlinear least-

squares regression applied to selections of manually-identified attached and separated flow, and separated-flow models are smoothed with a Laplacian smoother to ease the interpolation across β_e . In the Supplementary material, the four unique identified models in each aerodynamic coefficient are illustrated.

The final quasisteady functions required are the mixing parameter functions $p_{0,i}$. Figure 4 shows the estimates for these functions obtained by solving Eq. 3 for $p = p_0$ in the vicinity of the transition region. These estimates are given with respect to reference angles-of-attack, which are the centre-points of the attached flow regions, specified manually, and nonzero for nonzero β_e . A notable feature of these results is their asymmetry, with long tails at negative α (for $\beta_e < 0$). Phenomenologically, this is thought to arise from flow reattachment effects when both the control surface and the aerofoil are inclined, *e.g.*, upwards ($\beta_e < 0$, $\alpha > 0$), leading to a state in which the control surface itself is effectively at low angle-of-attack. Conversely, for $\beta_e < 0$, $\alpha < 0$, more rapid flow separation is expected, and is observed. The arctangent sigmoid of Reich [38] is not capable of capturing these asymmetric effects – instead, we utilise a modified logistic sigmoid. Its symmetric form, for the leading edge, is:

$$p_{0,l,i,\text{sym}}(\alpha_{l,i}) = S\left(\frac{1}{m_{l,i}}(|\alpha_{l,i} - \alpha_{l,i,\text{ref}}| - \psi_{l,i})\right), \quad S(x) = \frac{1}{1 + \exp(x)}, \quad (10)$$

where $S(x)$ is the logistic function, $\alpha_{l,i,\text{ref}}$ is the reference angle-of-attack (specified manually) and $m_{l,i}$ and $\psi_{l,i}$ are model parameters. The shift parameter $\psi_{l,i}$ is the α -value (w.r.t $\alpha_{l,i,\text{ref}}$) of the inflection or 50% point; that is $p_{0,l,i,\text{sym}}(\psi_{l,i} + \alpha_{l,i,\text{ref}}) = 0.5$. The width parameter $m_{l,i}$ governs the gradient at this point. The interpretability of these parameters aids identification. For the trailing edge ($p_{0,t,i}$), Eq. 10 applies directly; but to account for the asymmetric nature of the leading-edge mixing profiles in Fig. 4, a one-sided Gaussian function is added to Eq. 10, to yield the completed $p_{0,l,i}$:

$$p_{0,l,i}(\alpha_{l,i}) = \left(1 - p_{0,i,\text{sym}}(\alpha_{l,i})\right) G(\alpha_{l,i}) + p_{0,i,\text{sym}}(\alpha_{l,i}), \quad (11)$$

$$G(\alpha_{l,i}) = M_{l,i} \exp\left(-\left(\frac{\alpha_{l,i} - \alpha_{l,i,\text{ref}} + \psi_{l,i}}{w_{l,i}}\right)^2\right) [\alpha_{l,i} - \alpha_{l,i,\text{ref}} < 0]_{\text{IV}},$$

where $w_{l,i}$ and $M_{l,i}$ are model parameters, $\psi_{l,i}$ is the parameter identified in Eq. 10, and $[\cdot]_{\text{IV}}$ is the Iverson bracket [46], such that $[s]_{\text{IV}} = 1$ if s is true, and $[s]_{\text{IV}} = 0$ if s is false. The nature of this addition ensures that the resulting profile is smooth (C^∞) over the halfspaces $\alpha_{l,i} >$

$\alpha_{l,i,\text{ref}}$ and $\alpha_{l,i} < \alpha_{l,i,\text{ref}}$. The parameter $w_{l,i}$ governs the width of the Gaussian function, and the parameter $M_{l,i}$ its height.

For the four unique control surface deflections, leading- and trailing-edge parameters are estimated for $\beta_e = -50^\circ$ and $\beta_e = 0^\circ$; and a complete function over β_e is defined via linear interpolation. Table 2 shows these identified model parameters, including the associated interpolation index ($k \in [0, 1]$ for $\beta_e \in [-50, 0]^\circ$), and Fig. 4 the fitted p_0 functions. The parameter interpolation is linear and two-point ($k \in \{0, 1\}$), with the exception of $M_{l,i}$, which shows a rising trend with k but must necessarily be zero at $k = 1$ to preserve symmetry – to account for this, a non-monotonic piecewise-linear profile with the additional data-point $M_{l,i}(k = 0.75) = 0.6$ is used. These parameter variations are modelled at minimal complexity to maintain a reasonable level of model robustness and simplicity, consistent with the phenomenological nature of the model. We may then extend this model to $\beta_e > 0$ by symmetry, reconstruct complete quasisteady coefficient data, and validate it against the original data (Fig. 5). As can be seen, a generally good agreement is observed, despite some variation in the laminar-turbulent transition zones. We should note that the thin aerofoil at nonzero control surface deflection might be expected to show static hysteresis [44], but further studies are required to assess this. To our knowledge, this is the first modified GK model that accounts for control surface deflection – with the additional benefit of validity over the complete angle-of-attack envelope.

Table 2: Fitted model parameters for the logistic p_0 functions

Parameter	$\beta_e = -50^\circ$	$\beta_e = -30^\circ$	$\beta_e = -15^\circ$	$\beta_e = 0^\circ$
k	0	0.4	0.7	1
$\alpha_{l,i,\text{ref}}$	30.5°	19°	8°	0°
$\alpha_{t,i,\text{ref}}$	-148°	-162°	-172°	-180°
$m_{l,i}$	0.8	linear interpolation		3
$\psi_{l,i}$	4.4	linear interpolation		20
$M_{l,i}$	0.4	linear interp. via 0.6 at $0.75k$		0
$w_{l,i}$	18	linear interpolation		14
$m_{t,i}$	1.5	constant		1.5
$\psi_{t,i}$	11	linear interpolation		9

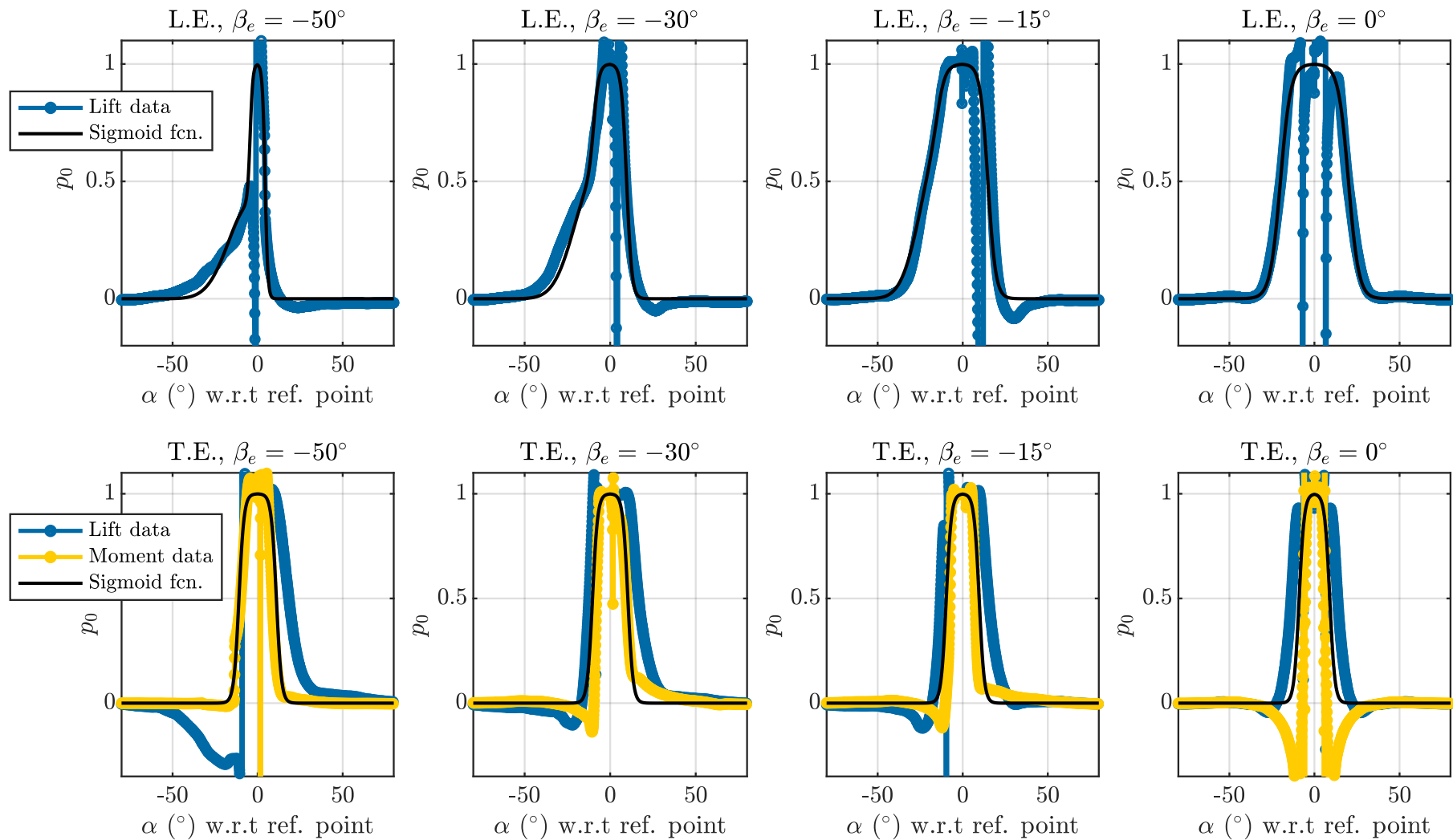


Figure 4: Unfiltered approximations to $p_{0,i}$ derived from stabiliser aerofoil (ST50H) leading edge (L.E.) and trailing edge (T.E.) aerodynamic data, against the associated logistic sigmoid fit.

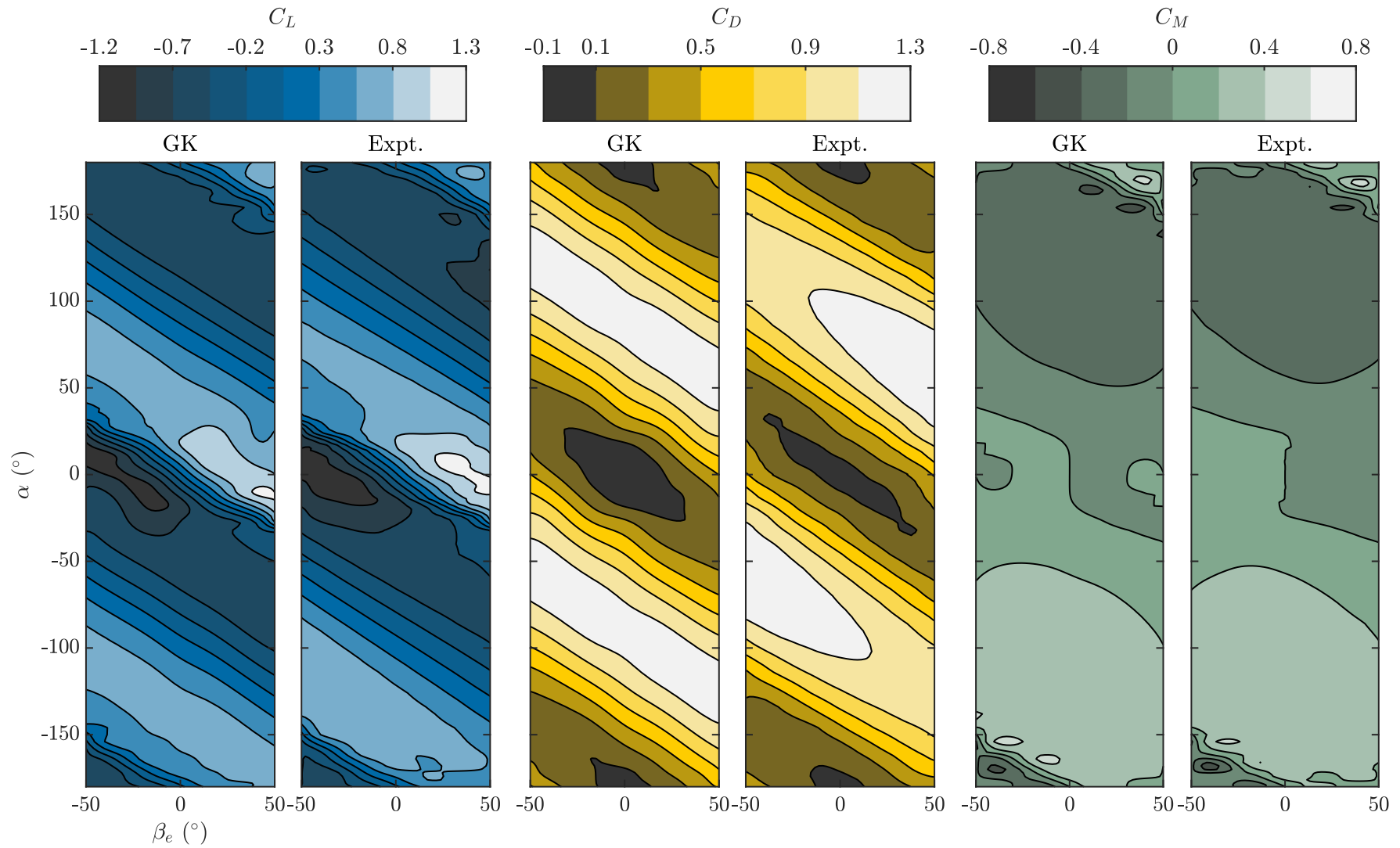


Figure 5: Quasisteady aerodynamic coefficient data for the stabiliser aerofoil (ST50H), as a function of both angle-of-attack (α) and control surface deflection (β_e), reconstructed from the GK attached and separated flow models, and compared to the original data.

3.4. Dynamic parameter identification

The only unidentified parameters now remaining in the GK model of the UAV are the transient delay parameters, $\tau_{1,i}$ and $\tau_{2,i}$, identifiable only from transient aerodynamic data. Within the literature a wide range of parameter values and relations are reported. Table 3 presents a comparison of $\tau_{1,i}$ and $\tau_{2,i}$ values for different aerofoils across the literature, expressed in dimensionless terms as factors of the convective time $t_{\text{conv}} = c/U$, for wing root chord c and freestream airspeed U in the context of wind-tunnel experiment. The full micro-air-vehicle identification of Uhlig and Selig [47] is also included, for reference. Delay parameters values are typically in the vicinity $\tau_{1,i} \approx \tau_{2,i} \approx 2t_{\text{conv}}$, though significant variation is observed even across identical aerofoil and similar Reynolds number.

Table 3: GK delay parameters reported in the literature.

Aerofoil	τ_1/t_{conv}	τ_2/t_{conv}	Source	Reynolds no.
NACA 0009	2.57	2.82	Williams <i>et al.</i> [44]	50,000
	3.6	4.3	Williams <i>et al.</i> [48]	57,000
	2.275	3.41	Reich <i>et al.</i> [38]	49,000
NACA 0012	1.13	0.316	Sedky <i>et al.</i> [49]	40,000
	2.01	1.50	Santra and Greenblatt [50]	240,000
NACA 0018	0.85	1.53	Williams <i>et al.</i> [51]	300,000
	0.25	3.6	Williams <i>et al.</i> [44]	250,000
	1.57	1.52	Greenblatt <i>et al.</i> [52]	300,000
Full micro-air-vehicle	2.46	0.384	Uhlig and Selig [47]	$\approx 25,000$

Recent developments in physics-based GK-model generalisation [53,54] indicate that this variation may be partially due to further parametric dependencies. Narsipur *et al.* [54] suggest that the stall delay effect, $\alpha_i - \tau_{2,i}\dot{\alpha}_i$ (Eq. 4), is better described by a delay with respect to a leading-edge suction parameter (LESP), computable from aerofoil geometry and aerodynamic conditions. Alternately, Ayancik and Mulleners [53] suggest both that the relaxation delay $\tau_{1,i}$ could be near-universal, with value $4.24t_{\text{conv}}$ for a wide range of aerofoils; and that the stall delay $\tau_{2,i}$ could be related to the pitch rate ($\dot{\alpha}$) and waveform of pitch motion, via near-universal correlation. These generalisations offer intriguing possibilities for physics-based GK models, but they are not yet at the point at which they can be directly utilised in state-space flight simulation models – for instance, the correlations proposed by Ayancik and Mulleners [53] rely on integral equations describing the delay parameter $\tau_{2,i}$. Nevertheless,

they suggest that the effects of aerofoil shape variation might be less significant than they appear. Following on from this, for the ST50W/H aerofoils used in the case study UAV, broadly comparable to NACA 0012, we utilise the results of the CFD simulations outlined in Pons and Cirak [36,43] to estimate $\tau_{1,i} = \tau_{2,i} = 2.3t_{\text{conv},i} = 2.3 c_i/U_i$ for the ST50W/H. Two model validity limits, in terms of local aerofoil motion transience, are defined. The maximum permissible reduced frequency is $\kappa_i = c_i\Omega_i/2U_i = 0.5$, where Ω_i is the frequency of local pitching motion; and the maximum permissible reduced pitch rate is $r_i = c_i\dot{\alpha}_i/2U_i = 0.13$. Furthermore, in our flight simulation framework, dimensional delay values ($\tau_{1,i}, \tau_{2,i}$) are taken to scale with c_i/U_i according to the variation in local induced flow U_i within a manoeuvre – with the topic of further scaling remaining open [53,54].

3.5. Combined model framework

The complete GK model now defines the aerodynamic submodel within the UAV flight dynamics ($\mathbf{f}(\cdot)$, Eq. 2). The combination of GK and multibody-dynamic models for the case study UAV lead to the complete state-space model:

$$\begin{aligned} & \begin{bmatrix} \mathbf{B}_1(\mathbf{z}, \mathbf{v}) & \\ & \mathbf{T}_1(\mathbf{z}, \mathbf{v}) \end{bmatrix} \begin{bmatrix} \dot{\mathbf{z}} \\ \dot{\mathbf{p}} \end{bmatrix} \\ & = \begin{bmatrix} \mathbf{f}(\mathbf{z}, \mathbf{p}, \mathbf{v}) \\ \mathbf{p}_0(\boldsymbol{\alpha}(\mathbf{z}, \mathbf{v}) - \mathbf{T}_2(\mathbf{z}, \mathbf{v})\dot{\boldsymbol{\alpha}}(\mathbf{z}, \mathbf{v})) \end{bmatrix} + \begin{bmatrix} -\mathbf{B}_0(\mathbf{z}, \mathbf{v}) & \\ & \mathbf{I} \end{bmatrix} \begin{bmatrix} \mathbf{z} \\ \mathbf{p} \end{bmatrix}, \end{aligned} \quad (13)$$

where the terms in \mathbf{p} and $\dot{\mathbf{p}}$ represent the flow attachment dynamics (Eq. 4) over all lifting surfaces, and the terms in \mathbf{z} and $\dot{\mathbf{z}}$ represent the UAV multibody dynamics (Eq. 2). The addition of the flow attachment dynamics significantly increases the size of the system under integration. Performing a mesh independence study indicates that five aerodynamic stations along each lifting surface is sufficient to converge overall lifting surface lift, drag and moment to within 1% for the manoeuvres we will study. This leads to an aerodynamic system ($\mathbf{p}, \dot{\mathbf{p}}$) with 25 degrees of freedom, in addition to the 12 degrees of freedom of the first-order multibody dynamics model ($\mathbf{z}, \dot{\mathbf{z}}$). We now apply this flight dynamic model to the design and understanding of supermanoeuvrability in the case study biomimetic UAV.

4. RaNPAS: the Pugachev cobra

4.1. Manoeuvre design

The Pugachev cobra is a pitch-axis RaNPAS supermanoeuvre, involving tilting the UAV backwards from level flight to beyond 90° pitch angle, and then forwards to level flight again, while maintaining approximately constant altitude [15,18]. While it is not observed in biological flight, it is available to a wide range of supermanoeuvrable aircraft. At the simplest level, performing a cobra manoeuvre in our biomimetic morphing-wing UAV requires the identification of three control configurations: **(i)** an initial trim configuration, **(ii)** a configuration to generate the moment required to pitch the UAV upwards to the partially inverted position; and **(iii)** a configuration to pitch the UAV forwards from the partially inverted position, and back to the trim configuration. We note that the trim configuration **(i)** is computable via existing methods [34]. This trim configuration may be a candidate for configuration **(iii)**, however, to find other more general candidates, we utilise a more general approach. Firstly, as the manoeuvre occurs within the vertical plane, the control space for manoeuvre design is constrained also by symmetry about this plane. Potential active control DOFs are thus the symmetric dihedral Γ , the symmetric sweep Λ , the symmetric incidence α , the elevator deflection β_e , and the thrust force F_{prop} . Some of these degrees of freedom are constrained: we enforce control limits on the elevator deflection ($|\beta_e| < 0.87$ rad, 50°) and wing sweep ($|\Lambda| < 1.171$ rad, 67°). Secondly, for initial manoeuvre design *only*, we utilise the original quasisteady aerodynamic model of this UAV [34] – to permit a characterisation of the UAV’s nonlinear longitudinal static stability profiles. We will optimise these profiles to generate candidate control configurations for the manoeuvre, which we will then test and verify under the transient (GK) aerodynamic model.

To generate candidate morphing configurations for the cobra manoeuvre, we define objective functions related to the intended behaviour of the configuration. For the pitch-up state, **(ii)** above, we use the pitch acceleration at a pitch value of 0.8 rad (46°), and use constrained least-squares optimisation to compute an optimal configuration for different set of morphing DOFs: for (A) all degrees of freedom active, (B) sweep and incidence active and (C) only incidence active. Figure 6 illustrates the optimal configurations generated by this optimisation, with DOF sets A-C indicated, alongside nonlinear longitudinal static stability plots for these configurations, that is, pitching acceleration $\ddot{\theta}(\theta)$ over pitch angle θ , for reference airspeed $U = 30$ m/s (approximately twice the stall speed of the unmorphed UAV

[36]) and $F_{\text{prop}} = 10 \text{ N}$ ($T/W = 0.13$). In these profiles, we may observe the location of the roots $\ddot{\theta}(\theta) = 0$, representing *quasi-trim* states: states momentarily at pitch equilibrium, and thus, the momentary stable orientation of the UAV. Parameter values for these three configurations are given in Table 4; values in bold type are located on their respective constraint limits – highlighting the effect of these constraints on the configuration performance. For example, in all states the elevator is at its control limit, and it is self-evident that increased elevator control effectiveness will result in greater pitch control effectiveness. In the fully-actuated UAV (A), the sweep degree of freedom is at its control limit, indicating that improvements in sweep control effectiveness (*e.g.*, via larger wing chord) would result in greater pitch control effectiveness. However, the Λ - α UAV, case (B), is not at any morphing control limits, indicating that more complex effects are also at play, for example the balance between the lift- and drag-generated pitch-up moment, and the optimisation trade-off that increased sweep represents for these two moments.

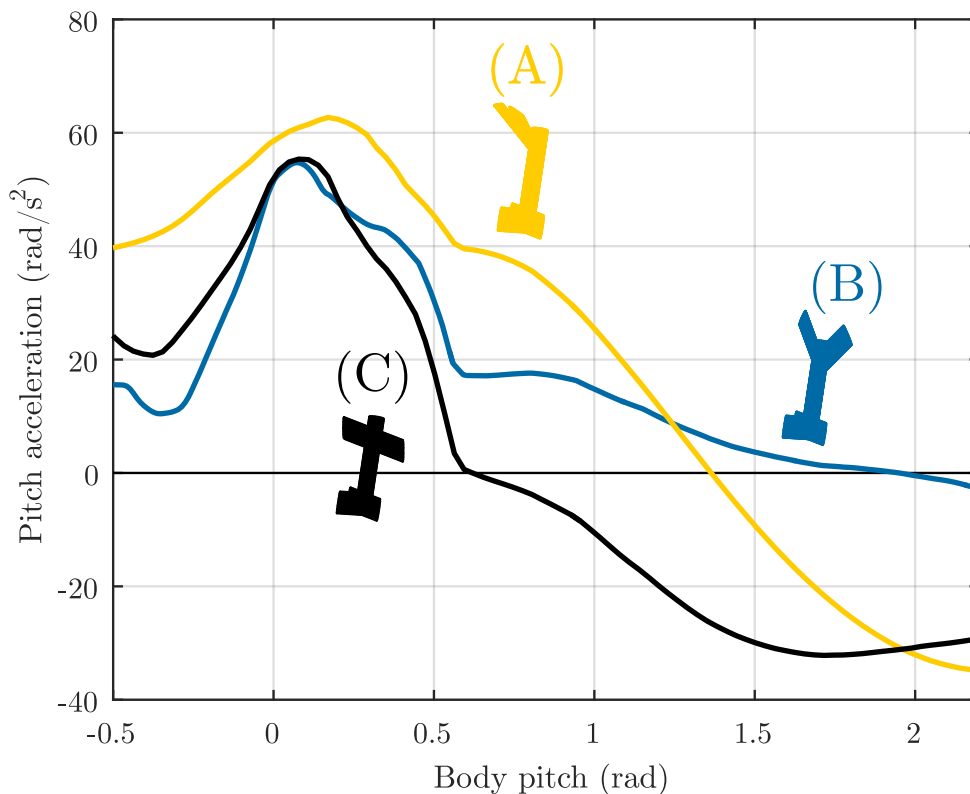


Figure 6: Static longitudinal stability profile of several candidate pitch-up configurations: (A) with all morphing DOF enabled; (B) with only sweep (Λ) and incidence (α) DOF enabled; (C) with only the incidence DOF enabled. The key feature of these profiles is the degree to which a positive (upwards) pitch acceleration is maintained at high angles of attack: the longer a positive acceleration is maintained, the greater the maximum attainable angle-of-attack during a RaNPAS manoeuvre.

Table 4: Parameters for candidate pitch-up configurations A-C. Values in bold type are located on their respective constraint limits.

Parameter	(A) All DOF	(B) Λ - α	(C) α
Γ (rad)	0.730	0	0
Λ (rad)	1.171	0.699	0
α (rad)	0.247	0.181	0.171
β_e (rad)	-0.870	-0.870	-0.870

The wing parameters associated with a high pitch-up rate are a positive dihedral, forward wing sweep and mild upwards inclination. Upwards inclination increases the wing lift, but too much reduces the drag-induced pitch-back moment at high angles of attack. Positive dihedral, in combination with forward sweep, induces a pitch-back drag moment even at low angles of attack. The forward sweep is particularly relevant, as this shifts the aerodynamic centre further forward and thus increases its pitching moment about the centre of mass (which is less strongly affected by the sweep motion). The result is that the UAV's stable pitch quasi-trim configuration is shifted to a very to a high angle of attack (in result (B), even to the partially-inverted position). While result (B) has a quasi-trim configuration at the highest angle of attack, the strength of its attraction is significantly weaker than that of result (A), as indicated by the pitch acceleration gradient at the quasi-trim configuration. Result (A) is thus likely to allow the cobra manoeuvre to be carried out more rapidly, and transient overshoot to the $\theta \approx 1.4$ rad quasi-trim state will take the UAV to higher angles. Note that the use of forward sweep in does have the disadvantage of decreasing the aeroelastic divergence speed of the wings [55], limiting the flight envelope of these forward-swept configurations.

For the pitch-down configuration, we use a similar objective function: Fig. 7 shows optimal configurations to minimise the pitch-down acceleration at 1.4 rad pitch, and Table 5 shows their parameter values. Results A-C are the optimal configurations for (A) all degrees of freedom active, (B) sweep and incidence active and (C) only incidence active. Result (D) is an example trim configuration, target pitch angle 0.08 rad – a non-optimal but obvious non-morphing candidate. Similar aerodynamic effects to those in Figure 6 are observed. Backward sweep moves the aerodynamic centre rearwards, and the presence of anhedral allows the maximum wing surface area to be inclined into the flow, maximising the restoring drag moment. In the swept cases, keeping the wing incidence flat makes use of this restoring drag moment; however, when only incidence motion is available, inclining the lifting surface into the local free-stream to reduce its drag is the better option – the tail then provides all the available restoring moment. This latter configuration has the additional benefit of generating

significant lift at high angles of attack, reducing the propulsive burden and/or altitude loss of the manoeuvre. The trim configuration itself, as a result of the airframe stability, generates moderate pitch-down acceleration; but this acceleration can be doubled in the presence of wing morphing.

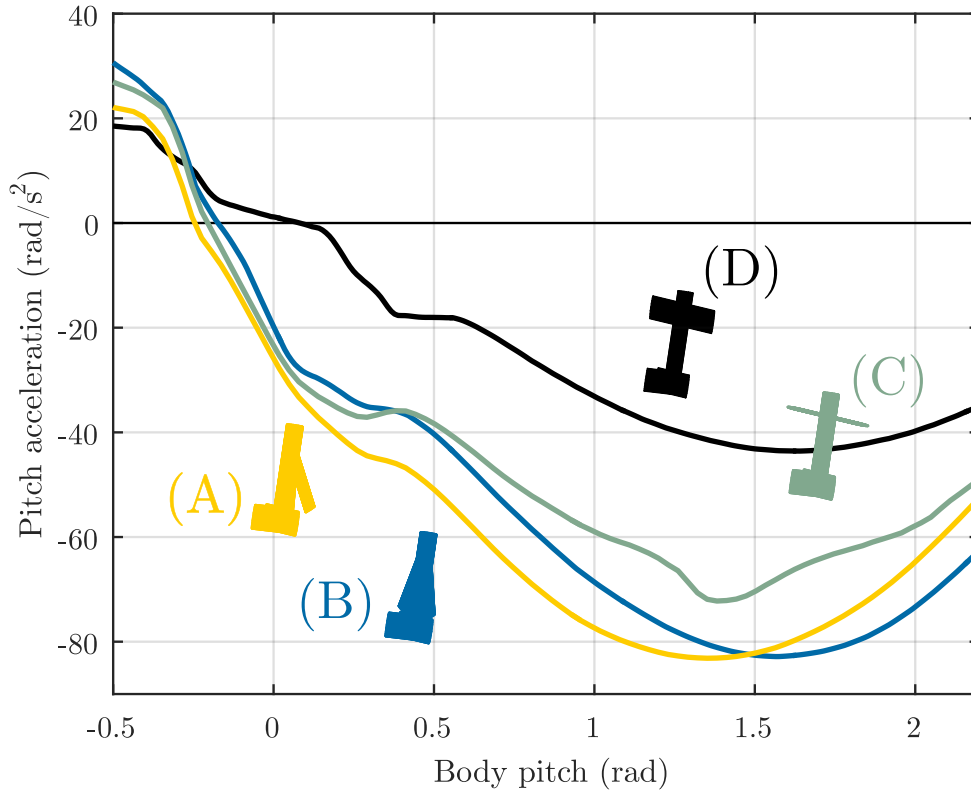


Figure 7: Static longitudinal stability profile of several candidate pitch-down configurations: (A) with all morphing DOF enabled; (B) with only sweep (Λ) and incidence (α) DOF enabled; (C) with only the incidence DOF enabled; (D) the initial trim configuration. The key feature of these profiles is the strength of the negative (downwards) pitch acceleration at high angles of attack ($> 90^\circ$): the greater the negative pitch acceleration, the more likely that the UAV can recover from a high-angle-of-attack states.

Table 5: Parameters for candidate pitch-down configurations A-D. Values in bold type are located on their respective constraint limits.

Parameter	(A) All DOF	(B) Λ - α	(C) α	(D) Trim
Γ (rad)	-0.255	0	0	0
Λ (rad)	-1.171	-1.171	0	0
α (rad)	0.168	0.0493	-1.654	0.014
β_e (rad)	0.262	0.262	0.262	0.003

4.2. Flight simulation of a 3DOF-morphing cobra manoeuvre

With candidate pitch-up and pitch-down configurations identified, we may simulate several forms of cobra manoeuvre. We start with the simplest to define: the UAV begins at a trim state; morphs to the all-DOF (3-DOF) pitch-up configuration (Fig. 6, Table 4); and then returns to the original trim state. In this manoeuvre, the only design variables that remain is the morphing timing, which we tune manually. Figure 8 shows the flight simulation results for a simple cobra manoeuvre of this form, including the UAV flight path, its control and orientation history, and its acceleration history compared with the quasistatic states (Fig. 6-7). This simulation is performed under the full GK aerodynamic model. The initial and final trim state is the state at pitch 0.08 rad and airspeed 30 m/s; with the UAV initialised at pitch 0.08 rad and airspeed 40 m/s; and a constant thrust at thrust-to-weight ratio of 0.25 throughout. The nominal morphing timings include 500 ms in the trim state, 100 ms transition, 50 ms in the trim-up state and then an immediate return to the trim state. These discontinuous morphing control signals are smoothed strongly via a Laplacian smoother, leading to the final smooth control commands used in Figure 8. The manoeuvre is successful: the UAV reaches a nose-up state ($\theta = 1.56$ rad, 89°) within half a second of the control onset, losing 19 m/s of airspeed in the process (a reduction of 46%). The UAV then regains airspeed as it transitions into a shallow dive, though not without notable pitch-down overshoot – reaching a nadir of -0.46 rad (-26°). The manoeuvre is roughly altitude neutral, as altitude gain due to the vertical thrust component at peak pitch offsets the altitude loss of the dive recovery. Finally, it is interesting to compare the dynamic pitch acceleration history of the UAV to the quasistatic nonlinear longitudinal stability profiles of the control configurations (Fig. 8D). During the early pitch-up manoeuvre, the quasistatic pitch-up configuration profile represents the dynamic profile relatively well, but, by the point of the peak pitch angle, the dynamic profiles differ significantly – a difference attributable to dynamic pitching effects and airspeed loss. Despite the difference, the manoeuvre is performed successfully, indicating that heuristics based on longitudinal stability profiles can be a successful strategy for designing supermanoeuvres in biomimetic UAVs, even with complex aerodynamic effects at work.

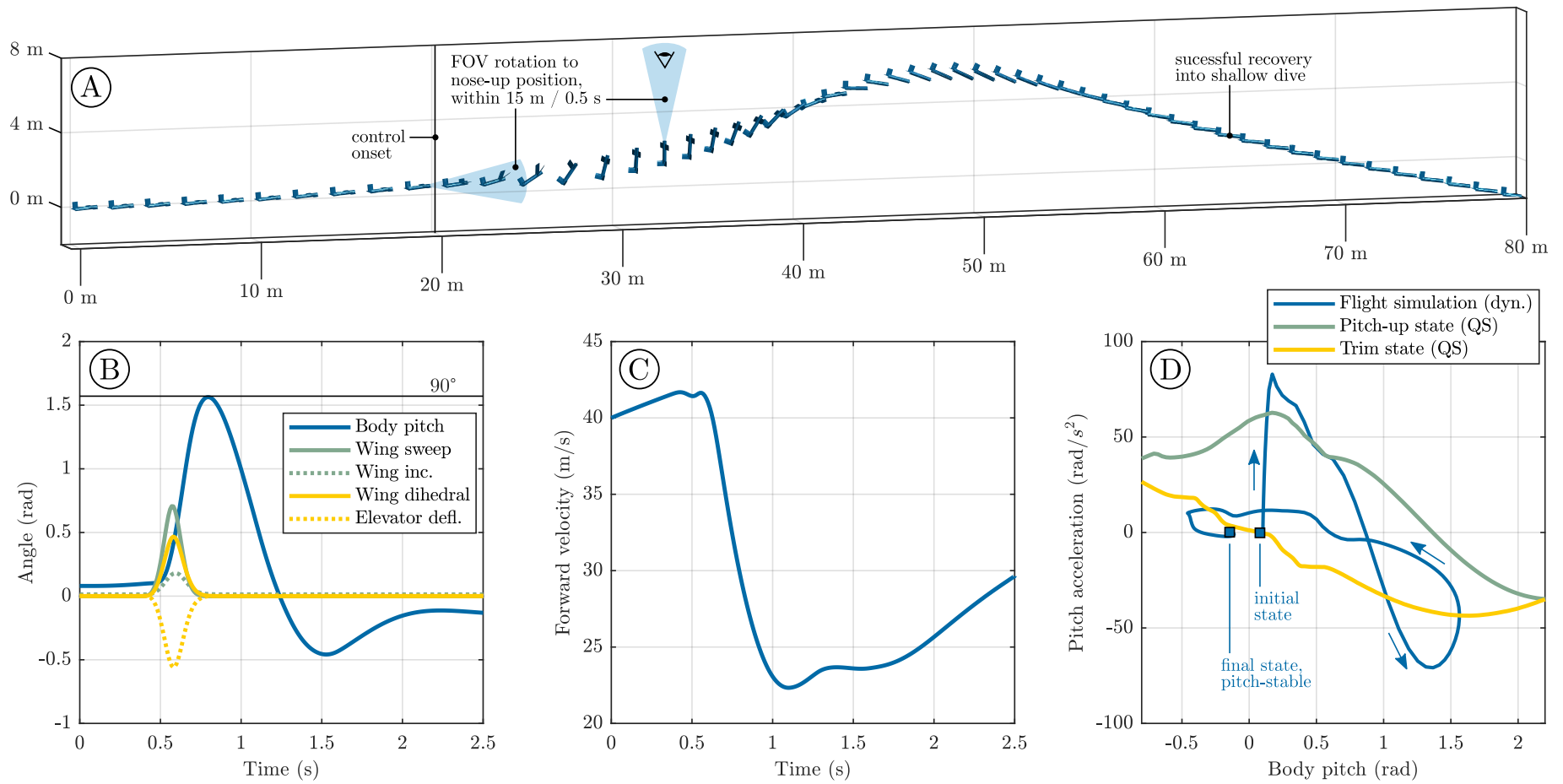


Figure 8: Flight simulation results for a simple 3DOF-morphing cobra manoeuvre at $T/W = 0.25$, under the GK aerodynamic model. (A) flight path with UAV rendered every 50 ms ($0 \leq t \leq 2.5$ s); (B) control and orientation history; (C) forward velocity history; and (D) acceleration history compared with the quasistatic acceleration profiles are shown. The UAV configuration sequence is: near-trim \rightarrow optimal pitchup \rightarrow near-trim.

4.3. Flight simulation of a 2DOF-morphing cobra manoeuvre

The cobra manoeuvre studied in §4.2 is high-performance, but requires 3DOF morphing – we are interested in reducing this morphing complexity, to make the manoeuvre more widely feasible. Considering the candidate configurations studied in §4.1 (Fig. 6-7), we observe that the 2DOF sweep-incidence (Λ - α) configuration can achieve similar levels of quasistatic pitching acceleration to the full 3DOF configuration. We observe, in particular, that it is the addition of sweep morphing that shifts the quasi-trim point of the pitch-up configuration (Fig. 6) to a point at greater than 90° pitch. Physically, forward motion of the UAV aerodynamic centre generates strong pitch-up moment based on lift force. In manoeuvre design terms, this bodes well for the prospect of a lower-DOF morphing cobra manoeuvre. However, simply chaining together the sweep-incidence candidate configurations in §4.1 does not lead to a successful manoeuvre: the pitch-up moment is insufficient to bring the UAV to beyond 90° pitch. Instead, we add another manoeuvre component. Previous analysis of this case study morphing-wing UAV [34] revealed the existence of a space of morphed UAV trim states across a window of pitch and yaw – steady level flight states at different fuselage orientations. To reduce the pitch-up moment requirement in the main stage of the manoeuvre, we use these morphed trim states to bring the UAV up to its maximum trim state pitch of 0.5 rad (29°) (Fig. 9), over a short duration. From this point we use the candidate pitch-up and pitch-down configurations of §4.1 to generate a cobra manoeuvre. This manoeuvre is successful: Fig. 9 shows the resulting set of cobra manoeuvres that can be achieved at differing initial airspeeds under the GK aerodynamic model. In several respects, these manoeuvres show better performance than the 3DOF manoeuvre (Fig. 8): they reach greater peak pitch (up to 1.95 rad, 112°), show minimal pitch-down overshoot during the recovery phase (down to only -0.096 rad, -5.5°), and lead to lower altitude loss. However, due to the initial trim-base reorientation, these manoeuvres are less rapid. This manoeuvre highlights the value of trim space analysis to the study of biomimetic supermanoeuvrability: trim space manoeuvres, or quasistatic NPAS (QNPAS) [34], can form an important component in rapid NPAS (RaNPAS).

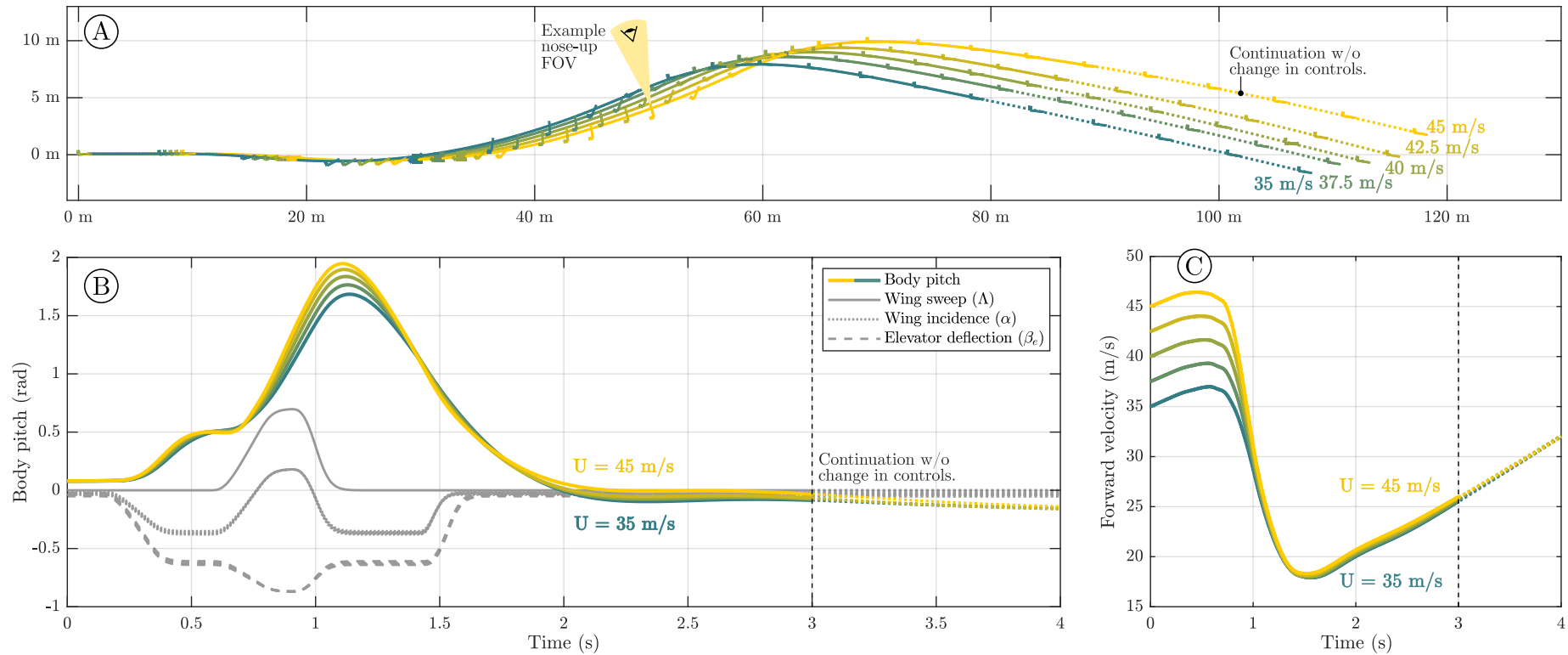


Figure 9: Flight simulation results for a 2DOF-morphing cobra manoeuvre at $T/W = 0.25$, with varying initial airspeed, and using the GK aerodynamic model. (A) flight path with UAV rendered every 200 ms ($0 \leq t \leq 4$ s); (B) control and orientation history; (C) forward velocity history. The UAV configuration sequence is: near-trim at $\alpha = 0$ rad \rightarrow trim at $\alpha = 0.4$ rad \rightarrow optimal pitchup \rightarrow trim at $\alpha = 0.4$ rad \rightarrow near-trim at $\alpha = 0$ rad. Beyond $t = 3$ s, the continued response of the UAV without changing control and morphing configuration (a shallow dive) is simulated, as an illustration of the post-manoeuve recovery process.

5. Biomimetic manoeuvrability: the ballistic transition

5.1. Motivation and manoeuvre design

RaNPAS manoeuvres such as the Pugachev Cobra have no direct parallels in biological supermanoeuvrability – perhaps, as a result of the close association between RaNPAS and equipment based on field-of-view (cannon, *etc.*) rather than on direct airframe contact (beaks, talons, *etc.*), *cf.* Fig. 1C. In biological creatures, true RaNPAS manoeuvres are likely of minimal utility, and thus have either not evolved or are not commonly observed. Nevertheless, some biological flight manoeuvres show correspondences with RaNPAS capability, though their motivation is not primarily to effect orientation changes. One such manoeuvre is the ballistic transition, observed in a variety of gliding mammals [11–13,29,31], and analogous to the deceleration phase of small-scale avian perching flight [3]. The ballistic transition manoeuvre is similar to a cobra manoeuvre, but with no pitch-down configuration: the objective is to decrease the airspeed of the organism in preparation for an impact landing on a vertical surface. As such, manoeuvre design for a ballistic transition manoeuvre in our case study biomimetic UAV can proceed along fundamentally the same lines as §4. We utilise a simple modification of the cobra controls established in §4.3: we generate a pitch-up moment via a 2DOF (Λ - α) morphing pitch-up configuration (Table 4, Fig. 6), but instead of transitioning subsequently to a pitch-down configuration, the UAV transitions to a neutral configuration which maintains a high pitch angle at decreasing airspeed until the point of impact. As a conveniently-located neutral configuration, we use the same pitch-up state but with zero incidence and elevator deflection (*i.e.*, only forward sweep). In a manoeuvre of maximum simplicity, this state may be maintained until impact landing – as we will now simulate.

5.2. Flight simulation

Figure 10 shows a simulation of a ballistic transition manoeuvre in the biomimetic UAV, under the GK aerodynamic model, and using the same 2DOF (Λ - α) sequence of configurations as in Fig. 6. The objective is a low-velocity impact landing of the UAV on the vertical surface of a building 45 m away, starting at forward velocity of 60 m/s. The effect of a varying the constant thrust value ($0.2 < T/W < 1$) is shown. For all simulated thrust values, the ballistic transition manoeuvre is successful, for a single set of control timings: the UAV lands very close to vertical orientation, and with both horizontal and vertical velocities below

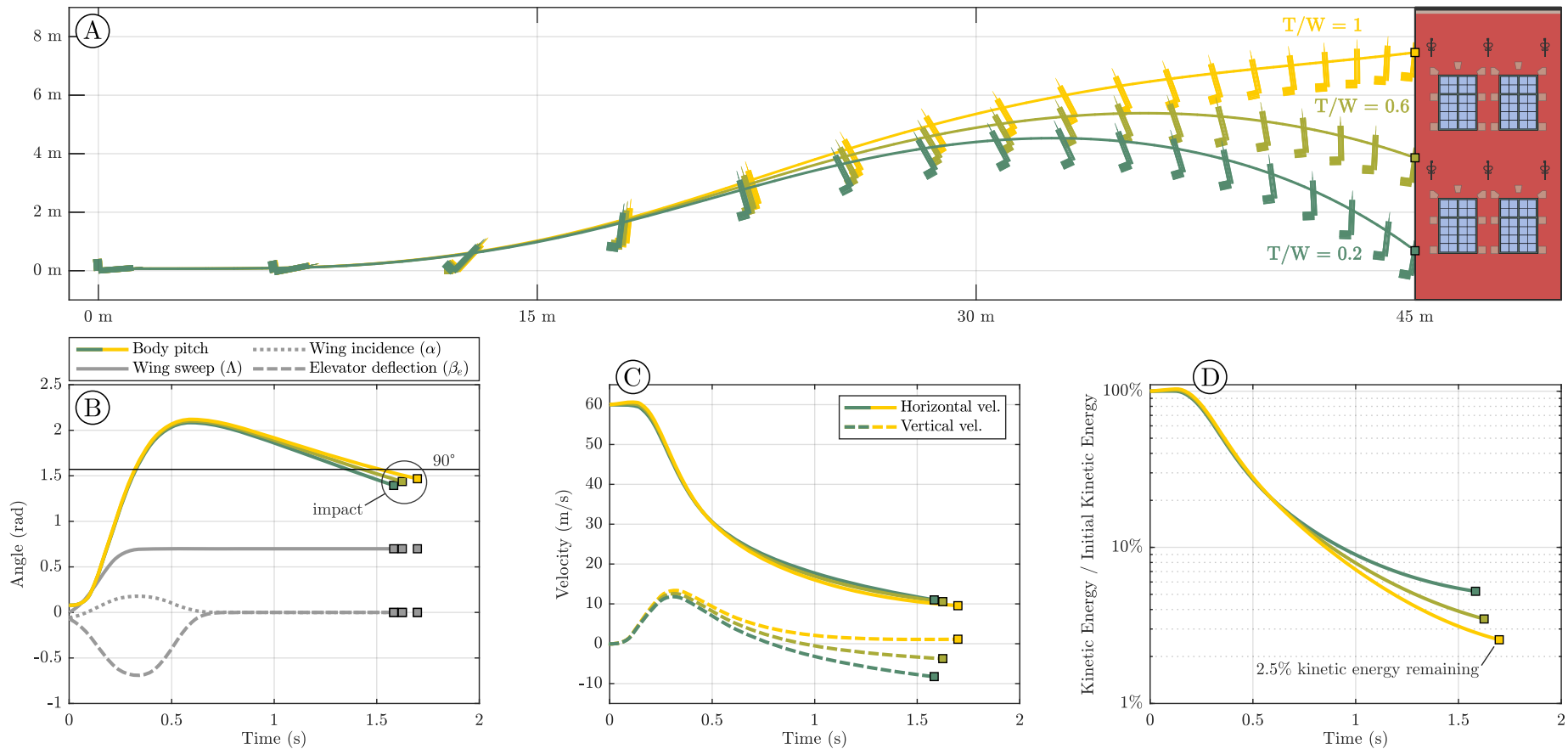


Figure 10: Flight simulation results for a 2DOF-morphing ballistic transition manoeuvre with initial velocity 60 m/s, under varying initial thrust (T/W). The UAV configuration sequence is: trim \rightarrow pitchup \rightarrow stabilisation state. **(A)** UAV flight paths, overlaid on an illustrative scenario involving landing on a building. **(B)** Body pitch angle histories and control histories, indicating the varying point of impact landing. **(C)** Horizontal and vertical velocity histories. **(D)** Relative kinetic energy history, indicating that in the best case ($T/W = 1$), the impact landing occurs with only 2.5% of the UAV's initial kinetic energy.

94% at the point of impact, with near-zero altitude change. The primary effect of T/W is to increase the altitude gain through the manoeuvre, reducing the UAV kinetic energy via transfer to gravitational potential. Maximal levels of kinetic energy dissipation (up to 97.5%) are thus associated with maximal available thrust (at least, up to $T/W = 1$). However, the effect of T/W on the aerodynamic energy dissipation is only secondary, as evidenced by the total energy trends: optimal total energy dissipation occurs at $T/W = 0.6$, but the variation is not large. The use of altitude gain for kinetic energy is useful but **(i)** may or may not be permissible in specific impact landing contexts, and **(ii)** may be achievable through finer morphing control at lower T/W. We note also that the use of forward sweep, and the corresponding reduction in wing aeroelastic divergence speed, might limit the initial airspeed of the manoeuvre: a more versatile manoeuvre sequence is to use incidence morphing (and, if available, dihedral) for initial airspeed reduction before a sweep morphing phase.

6. Effects of aerodynamic model fidelity

6.1. Model fidelity effects in a cobra manoeuvre context

The flight simulations in §§4-5 were performed with the modified GK dynamic stall model devised in §3: a model which captures the hysteretic effects of dynamic stall on all of the UAV's lifting surfaces. Two relevant questions can be formulated regarding the role of this model in the manoeuvres studied in §§4-5. Firstly: how significant are dynamic stall effects in these manoeuvres? And secondly: how do these manoeuvres fit into the ranges of model validity outlined in §3.4? Considering the simple 3DOF cobra manoeuvre of §4.2, Fig. 11 illustrates flight simulation results (pitch angle and flight path) for three different aerodynamic models: **i)** the quasisteady model based on original source data; **ii)** the GK-reconstructed quasisteady model, with $p = p_0$ (§§3.2-3.3); **iii)** the transient GK model with full dynamic stall effects. Figure 9 also illustrates the wing- and stabiliser-tip lift coefficient histories for the three simulations, and provides an assessment of the full transient GK simulation in terms of reduced frequency and reduced pitch rate, with the thresholds for GK model validity noted.

As can be seen, the cobra manoeuvre in this biomimetic UAV is remarkably resilient to dynamic stall effects: while these effects do cause significant changes in the manoeuvre lift coefficient peaks, these changes do not fundamentally alter the nature of the manoeuvre. A potential explanation for this resilience is that the near-symmetric nature of the dynamic stall hysteresis loop – with delayed stall and delayed reattachment – may serve to approximately self-cancel in a near-symmetric pitch-up/pitch-down manoeuvre. It may also be the case that

the relatively short-duration variations in aerodynamic coefficients (Fig. 11C) do not propagate to larger deviations in the manoeuvre as a result of the stability properties of the morphing configurations – *e.g.*, the strong static longitudinal stability of the 3DOF pitch-up configuration about its high-angle quasi-trim state (Fig. 6, configuration A). Hypothetically, strongly stable quasi-trim states might ensure convergence to these quasi-trim angles (at least, for the ≈ 1 s timescale of the manoeuvre) irrespective of the perturbations due to dynamic stall during pitch-up motion. And the same might be said of strongly stable pitch-down states, including the UAV's trim states. In §6.2, we will be able make limited tests of these hypotheses by comparing the effects of dynamic stall on the cobra manoeuvre to those on the ballistic transition manoeuvre.

However, prior to that we should briefly note that there are other unsteady aerodynamic effects *not* modelled in the UAV flight dynamic model that could have implications for manoeuvre control and/or feasibility. Attached-flow unsteady effects [55] have the potential to influence the behaviour of the rapid pre-stall motion during cobra manoeuvre onset. Low-order models are capable of modelling such effects [55], but these are difficult to integrate with dynamic stall models – further integration studies, or independent analysis of attached-flow segments of the manoeuvre are required to assess their implications for the manoeuvre. In addition, asymmetric forebody separation [56,57] has the potential to initiate roll- and yaw-drift away from the intended vertical plane of the manoeuvre. Higher-fidelity CFD and/or experimental approaches are required to resolve these separation effects, particularly in the novel context of a biomimetic UAV at relatively low Reynolds number – as opposed to the conventional context of a full-scale delta-wing aircraft [56,57]. The reduced-order simulations here indicate that these manoeuvres are likely aerodynamically viable in a biomimetic morphing-wing UAV, and thus motivate these higher-fidelity approaches.

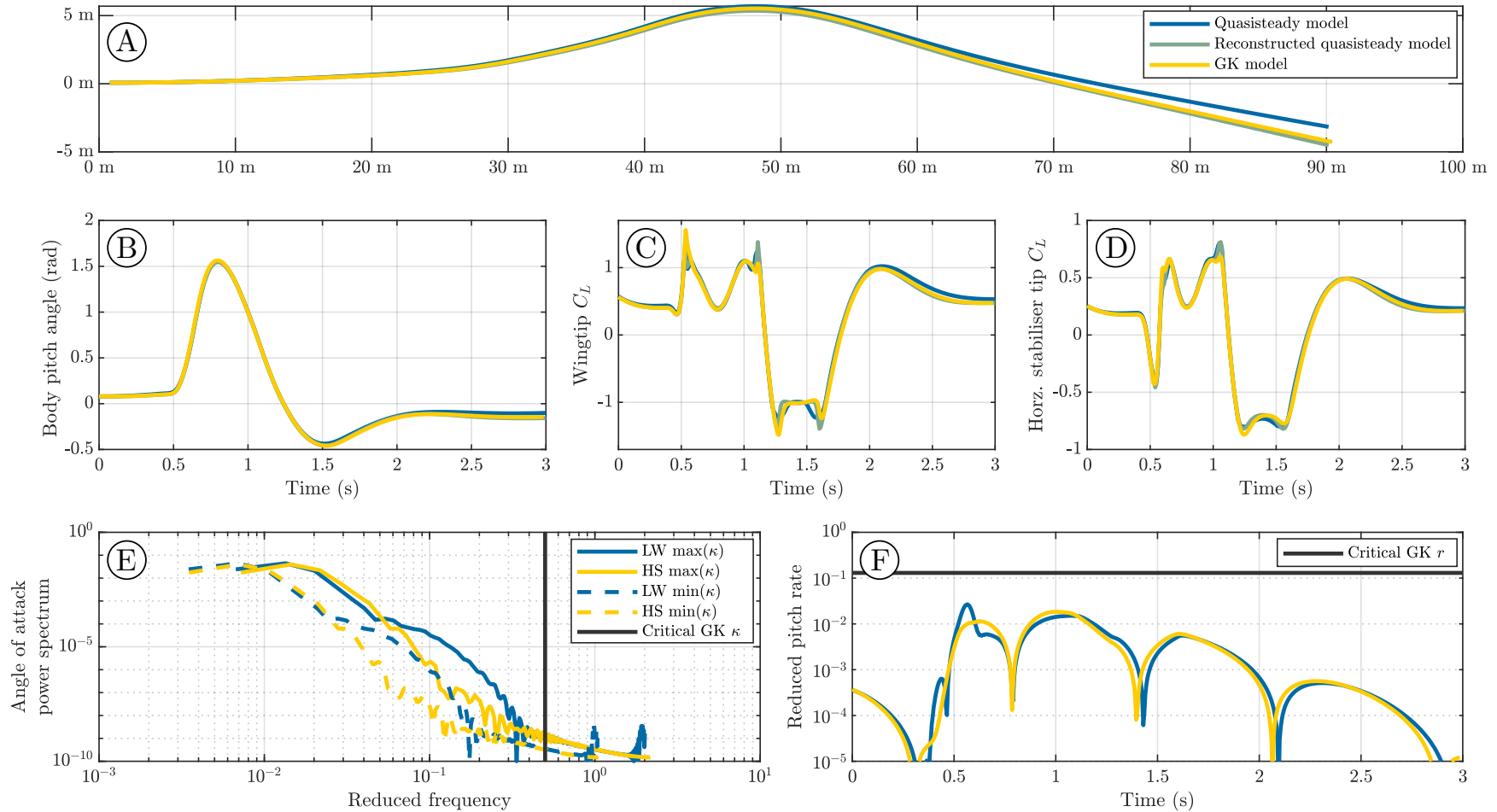


Figure 11: Validation flight simulation results for a simple 3DOF-morphing cobra manoeuvre at $T/W = 0.25$: simulations with the quasisteady aerodynamic model; with the GK-reconstructed quasisteady aerodynamic model; and with the GK model. **(A)** Flight path; **(B)** Orientation history; **(C)** Wingtip lift coefficient; **(D)** Horizontal stabiliser tip lift coefficient; **(E)** Angle of attack power spectrum, indicating the approximate limit of GK model validity. **(F)** Reduced pitch rate profile, indicating the approximate limit of GK model validity. As can be seen, the manoeuvre lies within the limits of GK model validity.

6.2. Model fidelity effects in a ballistic transition manoeuvre context

The fidelity analysis of §6.1 can also be applied to the ballistic transition manoeuvre of §5. Taking the highest-performance manoeuvre at $T/W = 1$, we perform the same three simulations: **i)** with the quasisteady aerodynamic model based on original source data; **ii)** with the GK-reconstructed quasisteady model, with $p = p_0$ (§§3.2-3.3); and **iii)** with the full transient GK model. Figure 12 shows the results of these simulations, including an assessment of the full transient GK simulation in terms of reduced frequency and reduced pitch rate, with the thresholds for GK and quasisteady model validity noted. The results are notably different to the cobra manoeuvre results of §6.1. The same short-duration differences in lift coefficient induced by dynamic stall are present, but in the ballistic transition manoeuvre, they propagate to significant differences in overall manoeuvre trajectory, and the UAV's kinematic energy at the point of impact landing. These changes are all the more interesting because the manoeuvre transience, as measured, for instance, by the reduced pitch rate, is lower than that of the cobra manoeuvres in §4. It is clear that whatever resilience the 3DOF cobra manoeuvre had to aerodynamic model fidelity is lessened substantially in the case of the 2DOF ballistic transition. This broadly supports the two hypotheses outlined in §6.1, but does not distinguish between them. On the one hand, the ballistic transition breaks the pitch-up/pitch-down symmetry of the cobra manoeuvre, and so delayed separation during pitch-up has no counteracting effect and is more likely to propagate to longer-term changes in flight path. On the other, the 2DOF pitch-up configuration has substantially lower static longitudinal stability in the vicinity of its quasi-trim point (Fig. 6), and thus less resilience to perturbation arising from dynamic stall. Further studies are required to discern the relative importance of these hypothetical mechanisms.

Finally, note that in the ballistic transition manoeuvre, the reduced frequency (κ) is not an ideal metric of lifting surface aerodynamic transience: the UAV airspeed changes significantly, leading to significant uncertainty in the value of the appropriate airspeed (U) used in the reduced frequency calculation ($\kappa = b\Omega/U$). Figure 12 shows only coarse estimates based on maximum and minimum airspeed. As a result of the time-frequency uncertainty principle [58], it is impossible to locate spectral components of a signal (Ω) precisely in time, and thus impossible to provide exact time-histories for reduced frequency κ . However, improvements over the current max-min approach may be available, via the use of short-time Fourier transforms [59]. This is a further topic which is relevant to the translation of GK modelling to real manoeuvre trajectories.

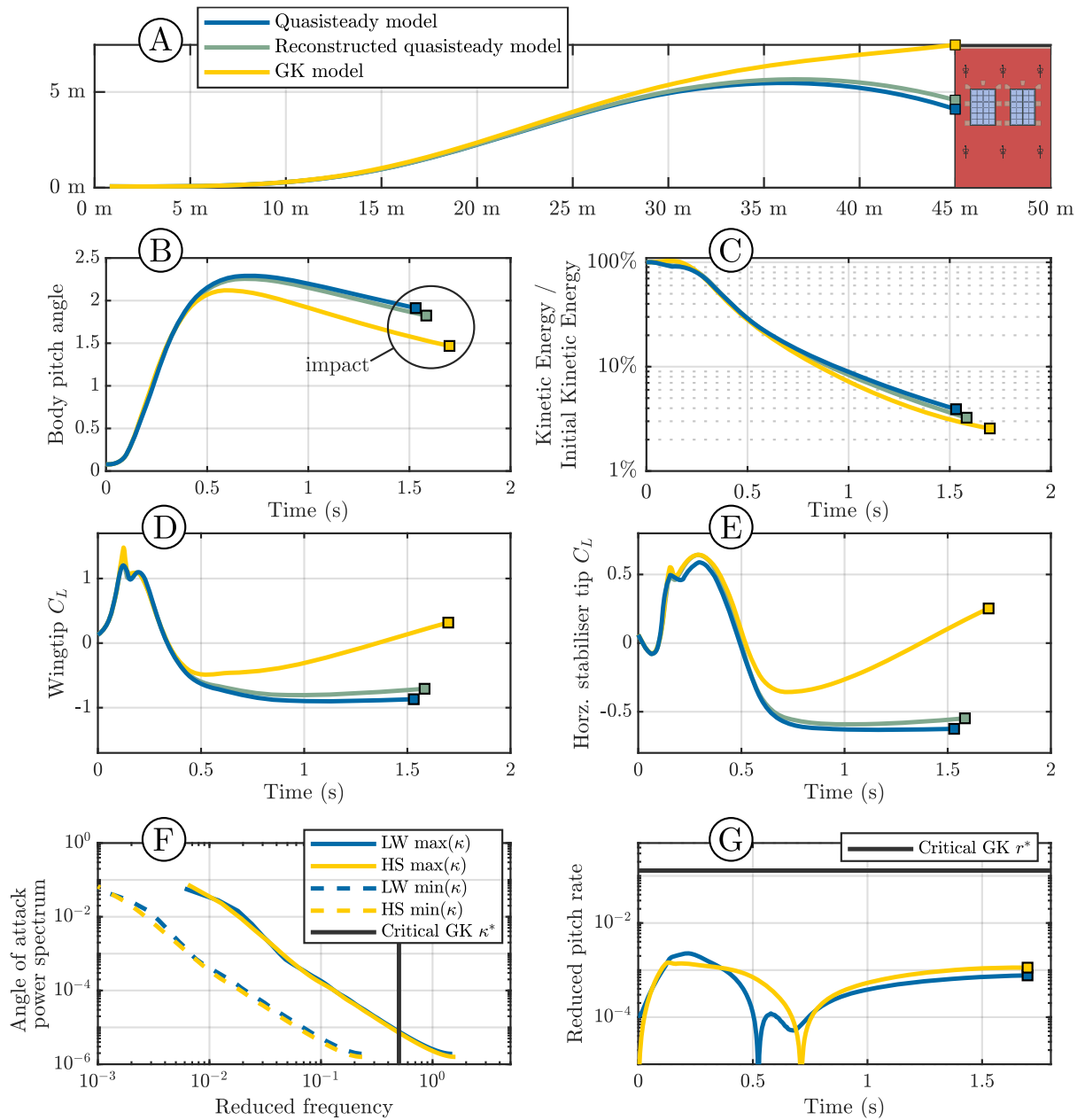


Figure 12: Validation flight simulation results for a ballistic transition manoeuvre at $T/W = 1$: simulations with the quasisteady (QS) aerodynamic model; with the GK-reconstructed quasisteady aerodynamic model; and with the full GK model. (A) Flight path; (B) Orientation history; (C) Relative kinetic energy history; (D) Wingtip lift coefficient; (E) Horizontal stabiliser tip lift coefficient; (F) Angle of attack power spectrum, indicating the approximate limit of GK model validity. (G) Reduced pitch rate profile, indicating the approximate limit of GK model validity.

7. Discussion and conclusion

In this work we have demonstrated in simulation that both classical and bio-inspired supermanoeuvrability is available in biomimetic morphing-wing UAVs. Pitch-axis RaNPAS, in the form of the cobra manoeuvre, is demonstrated using multiple forms of morphing control, and without thrust vectoring. Biomimetic ballistic transition manoeuvres, in imitation of the vertical landing manoeuvres of flying squirrels, is demonstrated via modification of cobra manoeuvre controls. The flight simulation system involves full multibody-dynamic models of biomimetic morphing; and state-of-the-art GK modelling of dynamic stall effects, including the first GK model of an aerofoil with a control surface. The simulation is subject to several limitations, including a neglect of out-of-plane aerodynamic effects such as asymmetric forebody separation, but it nevertheless demonstrates the principle of a biomimetic mechanism of supermanoeuvrability.

This biomimetic mechanism provides an impetus for several further directions of study. It motivates the development of supermanoeuvrable biomimetic UAVs – including UAVs capable of landing on vertical surfaces – as well as raising several practical open questions in this area. For instance: in what contexts is thrust-vectoring supermanoeuvrability preferable to morphing-wing supermanoeuvrability? Are there manoeuvres which are possible via one of these mechanisms, but not the other? We can already identify several hypothetical contexts in which the biomimetic mechanism of supermanoeuvrability might be preferable. This mechanism does not rely on thrust to effect orientation changes, and thus is accessible in low thrust-to-weight UAVs – and potentially at glide states. It may also be translatable to supermanoeuvrability in flapping-wing UAVs, through an extension of the manoeuvre design method based on longitudinal static stability to time-averaged flapping-wing static stability.

The biological connections to this biomimetic mechanism also deserve further exploration – both, in the identification of additional bio-inspired manoeuvres; and in the application of our analysis methods to the understanding of specifically biological manoeuvrability. With regard to the former, there is already extensive literature on stall turns [6–8] in birds and bats: the relationship between these turns and classical yaw-axis RaNPAS is an interesting further topic of research. With regard to the latter, there is already evidence that birds can transition between flight dynamic stability and instability via wing morphing [60], which ties into our observation that morphing-induced stability (and quasi-trim state) changes

are key to enabling biomimetic supermanoeuvrability. Recent studies into the flight dynamics and stability of flying squirrels [61] may provide avenues into assessing whether stability-driven mechanisms are also at work in cases of gliding supermanoeuvrability. The intersection between classical supermanoeuvrability, biological flight manoeuvrability, and biomimetic morphing-wing UAVs is a cross-disciplinary topic with the potential to significantly advance our understanding of the mechanisms of biological aerial manoeuvrability, and as well as enable enhancements in UAV manoeuvrability.

Declaration of competing interest

The authors declare that they have no known competing financial interests or personal relationships that could have appeared to influence the work reported in this paper.

References

- [1] KleinHeerenbrink M, France L A, Brighton C H and Taylor G K 2022 Optimization of avian perching manoeuvres *Nature* **607** 91–6 DOI: 10.1038/s41586-022-04861-4
- [2] Fernando J N and Rival D E 2017 On the dynamics of perching manoeuvres with low-aspect-ratio planforms *Bioinspir. Biomim.* **12** 046007 DOI: 10.1088/1748-3190/aa6f47
- [3] Polet D T and Rival D E 2015 Rapid area change in pitch-up manoeuvres of small perching birds *Bioinspir. Biomim.* **10** 066004 DOI: 10.1088/1748-3190/10/6/066004
- [4] Moore J, Cory R and Tedrake R 2014 Robust post-stall perching with a simple fixed-wing glider using LQR-Trees *Bioinspir. Biomim.* **9** 025013 DOI: 10.1088/1748-3182/9/2/025013
- [5] Carruthers A C, Thomas A L R, Walker S M and Taylor G K 2010 Mechanics and aerodynamics of perching manoeuvres in a large bird of prey *Aeronaut. J.* **114** 673–80 DOI: 10.1017/S0001924000004152
- [6] Gillies J A, Thomas A L R and Taylor G K 2011 Soaring and manoeuvring flight of a steppe eagle *Aquila nipalensis* *J. Avian Biol.* **42** 377–86 DOI: 10.1111/j.1600-048X.2011.05105.x
- [7] Tian X, Iriarte-Diaz J, Middleton K, Galvao R, Israeli E, Roemer A, Sullivan A, Song A, Swartz S and Breuer K 2006 Direct measurements of the kinematics and dynamics of bat flight *Bioinspir. Biomim.* **1** S10–8 DOI: 10.1088/1748-3182/1/4/S02
- [8] Windes P, Tafti D K and Müller R 2021 Kinematic and aerodynamic analysis of a bat performing a turning-ascending maneuver *Bioinspir. Biomim.* **16** 016019 DOI: 10.1088/1748-3190/abb78d

- [9] Sigrest P, Wu N and Inman D J 2023 Energy considerations and flow fields over whiffing-inspired wings *Bioinspir. Biomim.* **18** 046007 DOI: 10.1088/1748-3190/acd28f
- [10] Warrick D and Dial K P 1998 Kinematic, aerodynamic and anatomical mechanisms in the slow, maneuvering flight of pigeons *J. Exp. Biol.* **201** 655–72 DOI: 10.1242/jeb.201.5.655
- [11] Stafford B J, Thorington Jr. R W and Kawamichi T 2002 Gliding Behavior of Japanese Giant Flying Squirrels (*Petaurista Leucogenys*) *J. Mammal.* **83** 553–62 DOI: 10.1644/1545-1542(2002)083<0553:GBOJGF>2.0.CO;2
- [12] Byrnes G, Lim N T-L and Spence A J 2008 Take-off and landing kinetics of a free-ranging gliding mammal, the Malayan colugo (*Galeopterus variegatus*) *Proc. R. Soc. B Biol. Sci.* **275** 1007–13 DOI: 10.1098/rspb.2007.1684
- [13] Ando M and Shiraishi S 1993 Gliding flight in the Japanese giant flying squirrel *Petaurista leucogenys* *J. Mammal. Soc. Jpn.* **18** 19–32
- [14] Herbst W B 1980 Future fighter technologies *J. Aircr.* **17** 561–6 DOI: 10.2514/3.44674
- [15] Gal-Or B 2013 *Vectored Propulsion, Supermaneuverability and Robot Aircraft.* (New York, NY: Springer)
- [16] Joyce D A 2014 *Flying beyond the stall: the X-31 and the advent of supermaneuverability* (Washington, DC: NASA)
- [17] Erickson G E 1995 High Angle-of-Attack Aerodynamics *Annu. Rev. Fluid Mech.* **27** 45–88 DOI: 10.1146/annurev.fl.27.010195.000401
- [18] Ericsson L E 1995 Cobra maneuver unsteady aerodynamic considerations *J. Aircr.* **32** 214–6 DOI: 10.2514/3.46706
- [19] Nguyen Q-V and Chan W L 2018 Development and flight performance of a biologically-inspired tailless flapping-wing micro air vehicle with wing stroke plane modulation *Bioinspir. Biomim.* **14** 016015 DOI: 10.1088/1748-3190/aaefa0
- [20] Chirarattananon P, Ma K Y and Wood R J 2014 Adaptive control of a millimeter-scale flapping-wing robot *Bioinspir. Biomim.* **9** 025004 DOI: 10.1088/1748-3182/9/2/025004
- [21] Nan Y, Karásek M, Lalami M E and Preumont A 2017 Experimental optimization of wing shape for a hummingbird-like flapping wing micro air vehicle *Bioinspir. Biomim.* **12** 026010 DOI: 10.1088/1748-3190/aa5c9e
- [22] Keennon M, Klingebiel K and Won H 2012 Development of the Nano Hummingbird: A Tailless Flapping Wing Micro Air Vehicle *50th AIAA Aerospace Sciences Meeting including the New Horizons Forum and Aerospace Exposition* (Nashville, TN: AIAA)
- [23] Mackenzie D 2012 A Flapping of Wings *Science* **335** 1430–3 DOI: 10.1126/science.335.6075.1430

- [24] Kumar D, Goyal T, Kamle S, Mohite P M and Lau E M 2021 Realisation and testing of novel fully articulated bird-inspired flapping wings for efficient and agile UAVs *Aeronaut. J.* **125** 2114–48 DOI: 10.1017/aer.2021.55
- [25] Furst S J, Bunget G and Seelecke S 2013 Design and fabrication of a bat-inspired flapping-flight platform using shape memory alloy muscles and joints *Smart Mater. Struct.* **22** 014011 DOI: 10.1088/0964-1726/22/1/014011
- [26] Bie D, Li D, Xiang J, Li H, Kan Z and Sun Y 2021 Design, aerodynamic analysis and test flight of a bat-inspired tailless flapping wing unmanned aerial vehicle *Aerosp. Sci. Technol.* **112** 106557 DOI: 10.1016/j.ast.2021.106557
- [27] Zakaria M Y, Taha H E and Hajj M R 2015 Design Optimization of Flapping Ornithopters: The Pterosaur Replica in Forward Flight *J. Aircr.* 1–12 DOI: 10.2514/1.C033154
- [28] Zhang J, Zhao N and Qu F 2023 Bio-inspired flapping wing robots with foldable or deformable wings: a review *Bioinspir. Biomim.* **18** 011002 DOI: 10.1088/1748-3190/ac9ef5
- [29] Harris J M and Maloney K S 2010 *Petauroides volans* (Diprotodontia: Pseudocheiridae) *Mamm. Species* **42** 207–19 DOI: 10.1644/866.1
- [30] Bishop K L and Brim-Deforest W 2008 Kinematics of turning maneuvers in the southern flying squirrel, *Glaucomys volans* *J. Exp. Zool. Part Ecol. Genet. Physiol.* **309** 225–42 DOI: 10.1002/jez.447
- [31] Jackson S M 2000 Glide angle in the genus *Petaurus* and a review of gliding in mammals *Mammal Rev.* **30** 9–30 DOI: 10.1046/j.1365-2907.2000.00056.x
- [32] Evangelista D, Cam S, Huynh T, Kwong A, Mehrabani H, Tse K and Dudley R 2014 Shifts in stability and control effectiveness during evolution of Paraves support aerial maneuvering hypotheses for flight origins *PeerJ* **2** e632 DOI: 10.7717/peerj.632
- [33] Pope A P, Ide J S, Micovic D, Diaz H, Rosenbluth D, Ritholtz L, Twedt J C, Walker T T, Alcedo K and Javorssek D 2021 Hierarchical Reinforcement Learning for Air-to-Air Combat 2021 *International Conference on Unmanned Aircraft Systems (ICUAS)* (Athens, Greece: IEEE) pp 275–84
- [34] Pons A and Cirak F 2023 Multi-Axis Nose-Pointing-and-Shooting in a Biomimetic Morphing-Wing Aircraft *J. Guid. Control Dyn.* **46** 499–517 DOI: 10.2514/1.G006381
- [35] Pons A and Cirak F 2023 Quaternion Variational Integration for Inertial Maneuvering in a Biomimetic Unmanned Aerial Vehicle *ASME Lett. Dyn. Syst. Control* **3** 011008 DOI: 10.1115/1.4062685
- [36] Pons A 2019 *Supermanoeuvrability in a biomimetic morphing-wing aircraft* PhD Thesis (Cambridge, UK: University of Cambridge)

- [37] Dwivedi V and Damodaran M 2015 Computational Aeromechanics of a Manuevering Unmanned Aerial Vehicle with Variable-Incidence Wings *J. Aircr.* **52** 1914–26 DOI: 10.2514/1.C033102
- [38] Reich G W, Eastep F E, Altman A and Albertani R 2011 Transient Poststall Aerodynamic Modeling for Extreme Maneuvers in Micro Air Vehicles *J. Aircr.* **48** 403–11 DOI: 10.2514/1.C000278
- [39] Mi B, Zhan H and Lu S 2018 An extended unsteady aerodynamic model at high angles of attack *Aerosp. Sci. Technol.* **77** 788–801 DOI: 10.1016/j.ast.2018.03.035
- [40] Wickenheiser A M and Garcia E 2008 Optimization of Perching Maneuvers Through Vehicle Morphing *J. Guid. Control Dyn.* **31** 815–23 DOI: 10.2514/1.33819
- [41] Zhao J, Zeng L and Shao X 2023 A novel prediction method for unsteady aerodynamic force on three-dimensional folding wing aircraft *Aerosp. Sci. Technol.* **137** 108287 DOI: 10.1016/j.ast.2023.108287
- [42] Sabater C, Stürmer P and Bekemeyer P 2022 Fast Predictions of Aircraft Aerodynamics Using Deep-Learning Techniques *AIAA J.* **60** 5249–61 DOI: 10.2514/1.J061234
- [43] Pons A and Cirak F 2019 Three-Dimensional Flight Simulation with Transient Moving-Aerofoil Models *IUTAM Symposium on Recent Advances in Moving Boundary Problems in Mechanics* IUTAM Bookseries vol 34, ed S Gutschmidt, J N Hewett and M Sellier (Cham, Switzerland: Springer) pp 27–39
- [44] Williams D R, Reißner F, Greenblatt D, Müller-Vahl H and Strangfeld C 2017 Modeling Lift Hysteresis on Pitching Airfoils with a Modified Goman–Khrabrov Model *AIAA J.* **55** 403–9 DOI: 10.2514/1.J054937
- [45] Selig M 2010 Modeling Full-Envelope Aerodynamics of Small UAVs in Realtime *AIAA Atmospheric Flight Mechanics Conference* AIAA Atmospheric Flight Mechanics Conference (Toronto, Canada: AIAA)
- [46] Graham R L, Knuth D E and Patashnik O 1994 *Concrete mathematics: a foundation for computer science* (Reading, MA: Addison-Wesley)
- [47] Uhlig D V and Selig M S 2017 Modeling Micro Air Vehicle Aerodynamics in Unsteady High Angle-of-Attack Flight *J. Aircr.* **54** 1064–75 DOI: 10.2514/1.C033755
- [48] Williams D R, An X, Iliev S, King R and Reißner F 2015 Dynamic hysteresis control of lift on a pitching wing *Exp. Fluids* **56** 112 DOI: 10.1007/s00348-015-1982-y
- [49] Sedky G, Jones A R and Lagor F D 2020 Lift Regulation During Transverse Gust Encounters Using a Modified Goman–Khrabrov Model *AIAA J.* **58** 3788–98 DOI: 10.2514/1.J059127
- [50] Santra S and Greenblatt D 2021 Dynamic Stall Control Model for Pitching Airfoils with Slot Blowing *AIAA J.* **59** 400–4 DOI: 10.2514/1.J059818

- [51] Williams D R, Greenblatt D, Müller-Vahl H, Santra S and Reißner F 2019 Feed-Forward Dynamic Stall Control Model *AIAA J.* **57** 608–15 DOI: 10.2514/1.J057266
- [52] Greenblatt D, Mueller-Vahl H, Williams D R and Reissner F 2016 Goman-Khrabrov Model on a Pitching Airfoil with Flow Control *8th AIAA Flow Control Conference* 8th AIAA Flow Control Conference (Washington, DC: AIAA)
- [53] Ayancik F and Mulleners K 2022 All you need is time to generalise the Goman–Khrabrov dynamic stall model *J. Fluid Mech.* **942** R8 DOI: 10.1017/jfm.2022.381
- [54] Narsipur S, Gopalarathnam A and Edwards J R 2019 Low-Order Model for Prediction of Trailing-Edge Separation in Unsteady Flow *AIAA J.* **57** 191–207 DOI: 10.2514/1.J057132
- [55] Bisplinghoff R L, Ashley H and Halfman R L 1957 *Aeroelasticity* (Reading, MA: Addison-Wesley)
- [56] Ericsson L E and Beyers M E 2002 Forebody Flow Control at Conditions of Naturally Occurring Separation Asymmetry *J. Aircr.* **39** 252–61 DOI: 10.2514/2.2946
- [57] Bernhardt J E and Williams D R 1998 Proportional Control of Asymmetric Forebody Vortices *AIAA J.* **36** 2087–93 DOI: 10.2514/2.310
- [58] Cohen L 1995 *Time-frequency analysis* (Englewood Cliffs, NJ: Prentice Hall)
- [59] Durak L and Arikan O 2003 Short-time fourier transform: two fundamental properties and an optimal implementation *IEEE Trans. Signal Process.* **51** 1231–42 DOI: 10.1109/TSP.2003.810293
- [60] Harvey C, Baliga V B, Wong J C M, Altshuler D L and Inman D J 2022 Birds can transition between stable and unstable states via wing morphing *Nature* **603** 648–53 DOI: 10.1038/s41586-022-04477-8
- [61] Zhao F, Wang W, Zhang J, Wyrwa J and Sun F 2019 Aerodynamic Characteristics and Pitching Adjusting Mechanism of the Flying Squirrel With Deployed Patagium *IEEE Access* **7** 185554–64 DOI: 10.1109/ACCESS.2019.2961451